Computers & Geosciences 90 (2016) 40–56

Contents lists available at ScienceDirect

Computers & Geosciences

journal homepage: www.elsevier.com/locate/cageo

Reprint of: A numerical investigation of fine sediment resuspension in the wave boundary layer—Uncertainties in particle inertia and hindered settling ☆

Zhen Cheng [a,*], Xiao Yu [a], Tian-Jian Hsu [a], S. Balachandar [b]

[a] Center for Applied Coastal Research, University of Delaware, Newark 19716, DE, USA
[b] Mechanical and Aerospace Engineering, University of Florida, Gainesville 32611, FL, USA

ARTICLE INFO

Article history:
Received 1 January 2015
Received in revised form
15 June 2015
Accepted 18 July 2015
Available online 20 July 2015

Keywords:
Fine sediment transport
Inertia effect
Hindered settling
Gelling ignition

ABSTRACT

The wave bottom boundary layer is a major conduit delivering fine terrestrial sediments to continental margins. Hence, studying fine sediment resuspensions in the wave boundary layer is crucial to the understanding of various components of the earth system, such as carbon cycles. By assuming the settling velocity to be a constant in each simulation, previous turbulence-resolving numerical simulations reveal the existence of three transport modes in the wave boundary layer associated with sediment availabilities. As the sediment availability and hence the sediment-induced stable stratification increases, a sequence of transport modes, namely, (I) well-mixed transport, (II) formulation of lutocline resembling a two-layer system, and (III) completely laminarized transport are observed. In general, the settling velocity is a flow variable due to hindered settling and particle inertia effects. Present numerical simulations including the particle inertia suggest that for a typical wave condition in continental shelves, the effect of particle inertia is negligible. Through additional numerical experiments, we also confirm that the particle inertia tends (up to the Stokes number $St = 0.2$) to attenuate flow turbulence. On the other hand, for flocs with lower gelling concentrations, the hindered settling can play a key role in sustaining a large amount of suspended sediments and results in the laminarized transport (III). For the simulation with a very significant hindered settling effect due to a low gelling concentration, results also indicate the occurrence of gelling ignition, a state in which the erosion rate is always higher than the deposition rate. A sufficient condition for the occurrence of gelling ignition is hypothesized for a range of wave intensities as a function of sediment/floc properties and erodibility parameters.

1. Introduction

Fine sediments delivered by rivers are the main vehicle to carry terrestrial organic carbon, nutrients and anthropogenic contaminants to the ocean (e.g., Milliman and Farnsworth, 2011). According to Hedges et al. (1997), about 1.5×10^{14} g of particulate organic carbon (POC) is delivered to the ocean annually. However, only a very small amount of POC is preserved. Therefore, studying the fate of terrestrial sediment in continental margins, such as the physical mechanisms that control the delivery processes (e.g., Hale et al., 2014; Kniskern et al., 2014; Kolker et al., 2014) is one of the essential steps to better understand the global carbon cycle. The physical processes driving sediment source to sink are classified into three stages, namely, initial deposition, resuspension and final deposition (Wright and Nittrouer, 1995). Due to a variety of mechanisms associated with sediment-laden riverine outflow dynamics (e.g., trapping, flocculation), initial deposition of fine sediment is typically located within the inner-shelf (e.g., Geyer et al., 2000; Bever et al., 2011). Hence, resuspension can play a crucial role to further deliver fine sediment offshore. In the past decade, it has been well-established in many systems (e.g., Eel – Traykovski et al., 2000; Ogston et al., 2000; Po – Traykovski et al., 2007; Waiapu – Ma et al., 2008; Waipaoa – Hale et al., 2014) that during large wave events, concentrated fine sediment suspension can be maintained in the wave-current bottom boundary layer and the resulting high buoyancy anomaly drives offshore transport of fine sediment even over relatively mild shelf slopes. This process is referred to as the wave-supported sediment-driven gravity flow.

A high buoyancy anomaly is clearly prerequisite for offshore-directed gravity flow (Wright et al., 1988; Sternberg et al., 1996). Field observations by Traykovski et al. (2000, 2007) suggest that the occurrence of high buoyancy anomaly in fine sediment transport requires sufficiently strong turbulence as well as the formation of a lutocline, a sharp negative sediment concentration

☆This article is a reprint of a previously published article. For citation purposes, please use the original publication details: Computers & Geosciences, 83, pp. 176–192. DOI of original item: http://dx.doi.org/10.1016/j.cageo.2015.07.009.

* Corresponding author.
E-mail address: zcheng@udel.edu (Z. Cheng).

http://dx.doi.org/10.1016/j.cageo.2015.11.003
0098-3004/

gradient near the top of the wave boundary layer (Ross and Mehta, 1989). The existence of a lutocline indicates that the flow turbulence is suppressed by the sediment-induced stable density stratification, which effectively traps suspended sediments within a few centimeters near the bed, i.e., a form of convergence typically found during the formation of gravity flow (Ogston et al., 2000). Yet, the flow below the lutocline remains turbulent (Noh and Fernando, 1991; Trowbridge and Kineke, 1994) or at least transitionally turbulent (Ozdemir et al., 2010), so that the suspension is sufficiently mobile to drive gravity flows on mild slopes.

Due to interactions among descending particles, upward flow motions are generated and hence the collective settling velocity of particles is reduced from the single particle settling velocity. This is the well-known hindered settling effect (e.g., Winterwerp and Van Kesteren, 2004; Fredsoe and Deigaard, 1992). For non-cohesive sediments, hindered settling is a relatively well-constrained process (Richardson and Zaki, 1954; Jimenez and Madsen, 2003). For example, the reference concentration, often introduced in the hindered settling parameterization, is generally agreed to be the random-close-packing concentration of sediment (around 0.6 in terms of volumetric concentration). For fine sediments that often become cohesive in the coastal waters, the hindered settling plays a critical role in the slow deposition and consolidation processes. However, the parameterization of hindered settling for cohesive sediment is poorly constrained due to uncertainties in flocculation. When flocs are considered, the 'gelling concentration' is typically introduced to replace the reference concentration in the hindered settling parameterization (Dankers and Winterwerp, 2007), and it is defined as the concentration at which floc aggregates form concentrated aggregate networks (Winterwerp and Van Kesteren, 2004). However, the gelling concentration has a wide range of values due to variabilities in floc structures. For more organic and porous flocs with low fractal dimensions, the gelling concentration can be as low as ~100 g/L. In this case, Kampf and Myrow (2014) argue that the fine sediment transport in the bottom boundary layer can fall into a situation, called gelling ignition, in which the deposition flux is always lower than the erosion flux, and this gelling ignition will lead to a net increase of suspended sediment.

To understand fine sediment transport in the wave boundary layer due to episodic river floodings where the sediment supply is controlled by the river input, a series of three-dimensional (3D) turbulence-resolving numerical simulations based on a highly accurate pseudo-spectral scheme were carried out by Ozdemir et al. (2010) at the Stokes Reynolds number of $Re_\Delta = 1000$. This Re_Δ corresponds to a most energetic wave condition at Eel River inner shelf with near bed wave-induced velocity amplitude of 0.56 m/s and wave period of 10 s (Traykovski et al., 2000). With a prescribed/fixed amount of sediments in the domain in each simulation, model results demonstrated that the effect of sediment-induced density stratification is associated with the prescribed sediment load and the settling velocity, which leads to several distinct flow regimes. However, a more common scenario of sediment supply in the bottom boundary layer is due to the bottom resuspension/deposition where sediment availability is also a flow variable. Yu et al. (2013) developed a hybrid spectral-compact finite difference simulation model to study the fine sediment transport in the bottom boundary layer. Comparing to the pseudo-spectral scheme, this hybrid scheme is more flexible to incorporate variable viscosity, and nonlinear boundary conditions. Cheng et al. (2015) adopt this new scheme to study how a range of sediment/bed properties associated with resuspension can control the sediment availability and the resulting transport. Simulation results reveal that the sediment availability is highly dependent on the resuspension/deposition mechanism from/to the bed. Specifically, a decrease (increase) of critical shear stress of erosion or settling velocity causes a growth (reduction) of sediment availability and three distinct transport modes are revealed: transport mode I is of dilute, well-mixed sediment distribution where the attenuation of turbulence by sediments is negligible due to a low sediment concentration ($\ll$1 g/L); transport mode II is similar to the two-layer flow in stably stratified flow signified by the formation of lutocline due to moderate turbulence attenuation by sediment-induced density stratification. A high concentration mud suspension layer occurs near the bed with a typical layer thickness of not more than $O(10)$ cm; transport mode III is characterized by very significant attenuation of turbulence due to the presence of high sediment concentration which laminarizes the bottom boundary layer. As similar transport modes are observed in the field or in the laboratory (Traykovski et al., 2007; Lamb et al., 2004; Sahin et al., 2012; Traykovski et al., 2015), it is important to better quantify the occurrence of these transport modes because they directly control sediment fluxes. For example, the transport mode I is the familiar dilute suspension and the net transport is determined by the flux divergence of suspended load (Harris and Wiberg, 2002). When transport mode II occurs, large buoyancy anomaly caused by high suspended sediment concentration can encourage offshore delivery of fine sediments through gravity flows. When transport mode III occurs, it is believed that gravity flows may be terminated or maintained by gelling ignition due to the predominance of hindered settling effect (Kampf and Myrow, 2014).

In most of the numerical models for fine sediment transport, the particle velocity can be calculated by the equilibrium Eulerian approximation (Balachandar and Eaton, 2010), that is, a vectorial sum of the local fluid velocity, the settling velocity and additional particle inertia terms associated with the Stokes number. This approximation is only appropriate for particles of Stokes number much smaller than unity. From the theoretical perspective (Balachandar and Eaton, 2010), the particle inertia effect is another mechanism to deviate the particle velocity from the fluid velocity, especially in turbulent flows with high accelerations (Cantero et al., 2008). However, these additional terms are also ignored in the aforementioned turbulence-resolving studies. There is a need to quantify the effect of neglecting the particle inertia on fine sediment transport for typical wave conditions encountered in the continental shelves.

The purpose of this study is to evaluate and quantify the uncertainties associated with the parameterization of particle velocity of fine sediment transport in the wave boundary layer using a series of turbulence-resolving simulation. Model formulations are discussed in Section 2. The sensitivity of the particle inertial effect for typical energetic wave conditions in the inner-shelves is first evaluated (Section 3), and the effect of different degrees of hindered settling due to a range of gelling concentrations is then investigated in Section 4. Further discussions on the particle inertia effect on turbulence modulation and gelling ignition are presented in Section 5. Concluding remarks are given in Section 6.

2. Mathematical formulations

2.1. Governing equation

Following previous studies (Ozdemir et al., 2010; Cheng et al., 2015), the wave condition with a free-stream velocity magnitude $\widetilde{U}_0 = 0.56$ m/s and a wave period $\widetilde{T} = 10$ s is considered to represent a relatively energetic flow condition when fine sediments form high concentration suspensions on continental shelves (e.g., Traykovski et al., 2000). The Stokes boundary layer thickness is calculated to be $\widetilde{\Delta} = \sqrt{2\nu/\widetilde{\omega}} = 1.78$ mm, in which ν is the fluid kinematic viscosity and $\widetilde{\omega} = 2\pi/T$ is the wave angular frequency. The resulting Stokes Reynolds number is $Re_\Delta = \widetilde{U}_0\widetilde{\Delta}/\nu = 1000$. This

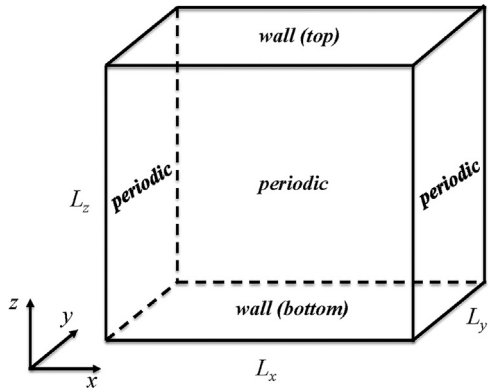

Fig. 1. Illustration of computation domain and coordinate system.

Stokes Reynolds number is in the range of intermittently turbulent flow where the fully turbulent condition can only be attained for a portion of the wave cycle (e.g., Jensen et al., 1989). The dimensional settling velocity is set to be $\widetilde{W}_{s0} = 0.5$ mm/s, which is typical for fine sediments in marine environments (Hill et al., 2000).

To generalize the simulation results, flow variables are non-dimensionalized and a set of dimensionless equations are solved in this study. We choose the free-stream velocity amplitude $\widetilde{U}_0$ as the characteristic velocity scale, and the Stokes boundary layer thickness $\widetilde{\Delta}$ as the characteristic length scale. Consequently, the characteristic time scale of fluid flow is calculated as $\tilde{t}_l = \widetilde{\Delta}/\widetilde{U}_0$. Hence, the non-dimensional flow variables are defined as

$$x_i = \frac{\tilde{x}_i}{\widetilde{\Delta}}, \quad t = \frac{\tilde{t}}{\tilde{t}_l}, \quad u_i = \frac{\tilde{u}_i}{\widetilde{U}_0}, \quad u_i^s = \frac{\tilde{u}_i^s}{\widetilde{U}_0}, \quad W_{s0} = \frac{\widetilde{W}_{s0}}{\widetilde{U}_0}, \quad p = \frac{\tilde{p}}{\rho_f \widetilde{U}_0^2}. \tag{1}$$

where $\tilde{p}$ is the dynamic pressure, ρ_f is the fluid density, $\tilde{u}_i$, $\tilde{u}_i^s$ are the non-dimensional fluid and sediment velocities, respectively, and $i = 1, 2, 3$ represents streamwise (x), spanwise (y) and vertical (z) components, respectively (see Fig. 1). In this paper, except for physical constants such as ρ_f, ν, and the gravitational acceleration g, variables without overhead '~' are non-dimensional variables.

In particle-laden turbulent flows, the degree of coupling between the carrier flow and dispersed particles is often characterized by comparing the characteristic time scale of fluid flow $\tilde{t}_l$ with the particle response time $\tilde{t}_p$, which is defined as

$$\tilde{t}_p = \frac{s\tilde{d}^2}{18\nu}, \tag{2}$$

where $s = \rho_s/\rho_f$ is the particle specific gravity, ρ_s is the sediment density, and $\tilde{d}$ is the particle diameter. When $\tilde{t}_p$ is relatively small compared with $\tilde{t}_l$, the equilibrium Eulerian approximation (Balachandar and Eaton, 2010) can be applied. Thus, the particle velocity u_i^s can be simplified to be an algebraic sum of the fluid velocity u_i, the settling velocity W_{s0} and an expansion in terms of the particle Stokes number St:

$$u_i^s = u_i - W_{s0}\delta_{i3} - St\left(1 - \frac{1}{s}\right)\frac{Du_i}{Dt} + O(St), \tag{3}$$

where the particle Stokes number $St = \tilde{t}_p/\tilde{t}_l$ is introduced to quantify the particle inertia relative to the flow inertia.

By substituting Eq. (3) into the Eulerian two-phase equations for the fluid phase (Cantero et al., 2008), and adopting the Boussinesq approximation, which is appropriate for the relatively small volumetric concentration of suspended fine sediment on continental shelves (Traykovski et al., 2007), the resulting non-dimensional continuity and momentum equations of the fluid phase are written as (Cheng et al., 2015)

$$\frac{\partial u_i}{\partial x_i} = 0, \tag{4}$$

$$\frac{\partial u_i}{\partial t} + u_j\frac{\partial u_i}{\partial x_j} = -\frac{\partial p}{\partial x_i} - \frac{2}{Re_\Delta}\sin\left(\frac{2t}{Re_\Delta}\right)\delta_{i1} + \frac{1}{Re_\Delta}\frac{\partial^2 u_i}{\partial x_j \partial x_j} - \frac{1}{Fr^2}\phi\delta_{i3}, \tag{5}$$

where the second term on the right-hand-side of Eq. (5) represents the streamwise pressure gradient that drives the prescribed wave motion. The last term on the right-hand-side of Eq. (5) results from the momentum exchange between the sediment phase and the carrier fluid with ϕ representing the volumetric concentration of sediment and the particle Froude number $Fr = \widetilde{U}_0/\sqrt{(s-1)g\widetilde{\Delta}}$ is also introduced. For the bottom resuspension, this term typically represents sediment-induced stable density stratification, which can attenuate the carrier flow turbulence (Cheng et al., 2015).

The non-dimensional mass conservation equation of the sediment phase is written as

$$\frac{\partial \phi}{\partial t} + \frac{\partial \phi u_i^s}{\partial x_i} = \frac{1}{Re_\Delta\, Sc}\frac{\partial^2 \phi}{\partial x_i \partial x_i}, \tag{6}$$

where $Sc = \nu/\kappa$ is the Schmidt number with κ denoting the sediment diffusivity. The Schmidt number is chosen to be $Sc = 0.5$ in this study (Ozdemir et al., 2010; Yu et al., 2013).

The bottom boundary layer is idealized to be statistically homogeneous in streamwise (x) and spanwise (y) directions (see Fig. 1). Periodic boundary conditions are used along streamwise and spanwise boundaries for fluid phase velocities and the sediment concentration. Two walls are located at the top and bottom boundaries and no-slip and no-penetration wall boundary conditions are implemented for the fluid velocity. For the sediment concentration, a no-flux boundary condition is applied at the top boundary:

$$w^s\phi - \frac{1}{Re_\Delta\, Sc}\frac{\partial \phi}{\partial z}\bigg|_{z=L_z} = 0, \tag{7}$$

where $z = L_z$ is located at the top of the domain, and w^s is the vertical component of the sediment velocity.

At the bottom boundary, an erodible/depositional boundary condition is implemented for sediment concentration to allow resuspension/deposition at the bottom:

$$w^s\phi - \frac{1}{Re_\Delta\, Sc}\frac{\partial \phi}{\partial z}\bigg|_{z=0} = E - D, \tag{8}$$

where E and D are non-dimensional erosional and depositional fluxes from/to the bottom, respectively, and both E and D are nondimensionalized by the free-stream velocity magnitude $\widetilde{U}_0$. The continuous non-dimensional depositional flux is specified as (Sanford and Maa, 2001; Winterwerp, 2007)

$$D = -w^s\phi|_{z=0}. \tag{9}$$

The non-dimensional erosion rate E is calculated by the Partheniades-Ariathurai type formulation (e.g., Sanford and Maa, 2001):

$$E = \begin{cases} m_e\left(\dfrac{|\tau_b|}{\tau_c} - 1\right), & |\tau_b| \geq \tau_c \\ 0, & |\tau_b| < \tau_c \end{cases}, \tag{10}$$

where m_e is the non-dimensional empirical coefficient of erosion rate (normalized by $\widetilde{U}_0$), τ_b is the non-dimensional bottom shear stress and the non-dimensional critical shear stress of

erosion is represented by τ_c. Both τ_b and τ_c are normalized by $\rho_f \widetilde{U}_0^2$.

2.2. Numerical implementation

In this study, the computational domain (see Fig. 1) is kept the same as the previous study of Ozdemir et al. (2010), which is $\widetilde{L}_x \times \widetilde{L}_y \times \widetilde{L}_z = 60\widetilde{\Delta} \times 30\widetilde{\Delta} \times 60\widetilde{\Delta}$, and it has been shown to be sufficient to resolve the largest turbulent eddies at the Stokes Reynolds number of $Re_\Delta = 1000$. Following Cheng et al. (2015), the model domain is discretized into $N_x \times N_y \times N_z = 128 \times 128 \times 257$ with uniform grids in both streamwise and spanwise directions, and Chebyshev collocation points are used in the vertical direction. A more detailed discussion is given later to demonstrate that the present numerical resolution is sufficient. Taking advantage of the statistical homogeneity in the streamwise (x) and spanwise (y) directions, ensemble-averaged (turbulence-averaged) flow quantities can be calculated approximately by averaging over the x–y plane.

A hybrid numerical scheme which maintains Fourier expansions in homogeneous directions (streamwise and spanwise) and implements sixth-order centered compact finite difference method in the wall-normal direction (Yu et al., 2013) is utilized in this study. With this hybrid scheme, flow-dependent properties and more flexible boundary conditions become relatively straightforward to implement. Uniform grids are used in the two homogeneous directions and Chebyshev collocation points are used in the vertical direction in order to better resolve the flow near the wall/bed. Eqs. (4) and (5) are solved with a standard projection method (Chorin, 1968). The velocity field is first advanced to the intermediate level. For diffusion terms, the Crank–Nicolson scheme is used. Nonlinear advection terms are calculated by the Arakawa method (Arakawa and Lamb, 1981) with the 2/3 dealiasing law. To preserve the accuracy of the 128 grids used in the x and y directions, the nonlinear products are computed on 192 grids, while 128 unfiltered wave-numbers are retained. The temporal integration is performed using a third-order low-storage Runge–Kutta scheme. A direct solver is used to solve the pressure Poisson equation, and once the pressure is determined, the intermediate velocity field is corrected to satisfy Eq. (4). For the sediment concentration equation, similar numerical scheme are used. More detailed discussions on the numerical schemes and implementations can be found in Cortese and Balachandar (1995) and Yu et al. (2013). The implementation of the top boundary condition (Eq. (7)) is discussed in detail in Appendix A.

Yu et al. (2014) used the same grid resolution and domain size as in the present study, and demonstrated that it is sufficient to reproduce the DNS results of clear fluid oscillatory wave boundary layer at $Re_\Delta = 1000$in Spalart and Baldwin (1989). An additional evidence for sediment-laden condition is given here using Case 0 (see Table 1). The grid resolution can be verified by comparing

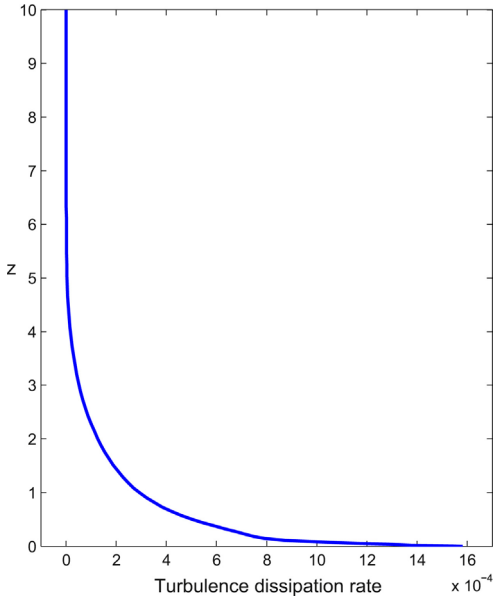

Fig. 2. Simulation results of turbulence dissipation rate at the flow peak for Case 0.

with the Kolmogorov length scale, which can be estimated from the simulation results of turbulence dissipation rate. Fig. 2 shows the turbulence dissipation rate during the flow peak, the moment that the turbulence dissipation rate is the largest throughout the wave cycle. We can observe that the maximum non-dimensional turbulence dissipation rate ϵ occurs very close to the bed, which is about 1.6×10^{-3}. Therefore, the smallest non-dimensional Kolmogorov length scale is estimated to be about $\eta = (1/(\epsilon\, Re_\Delta^3))^{1/4} = 2.8 \times 10^{-2}$. According to Pope (2000), $l = 60\eta$ is the length scale representing the upper bound of dissipative ranges. We can verify that the non-dimensional grid size adopted here dx=0.47 is only about 28% of $l = 60\eta$. Hence, we verify that the grid resolution can capture sufficient turbulence scales for the cases considered in this study.

2.3. Simulation setup

In the previous studies (Ozdemir et al., 2010; Cheng et al., 2015), the inertia terms associated with the particle Stokes number St in the particle velocity expression (Eq. (3)) are neglected by assuming that the Stokes number St is sufficiently small, and the particle velocity is calculated as

$$u_i^s = u_i - W_{s0}\delta_{i3}. \tag{11}$$

The dimensional settling velocity $\widetilde{W}_{s0}$ is calculated via the Stokes drag law:

Table 1
List of simulations presented in this study.[a]

Case	St	ϕ_{ref}	$\tilde{d}$ (μm)	$\widetilde{D}_f$ (μm)	n_f	$\bar{\tilde{\tau}}_{eq}$ (Pa)	$\bar{\Phi}_{eq}$	ϕ_{max}	Transport mode
0	NA	NA	24	NA	NA	0.39	1.76×10^{-3}	0.012	II
*A*1	0.03	NA	24	NA	NA	0.38	1.8×10^{-3}	0.013	II
*A*2	0.1	NA	NA	NA	NA	NA	*NA*	NA	II
*A*3	0.2	NA	NA	NA	NA	NA	NA	NA	III
*B*1	NA	0.63	24	NA	NA	0.38	1.95×10^{-3}	0.014	II
*B*2	NA	0.2	4	52.7	2.38	0.28	4.7×10^{-4}	0.021	III
*B*3	NA	0.13	4	66.6	2.27	0.28	7.0×10^{-4}	0.026	III
*B*4	NA	0.05	4	107.3	2.09	0.28	NA	0.05	III

[a] All simulations presented in this study are corresponding to non-dimensional parameters $Re_\Delta = 1000$, $W_{s0} = 9 \times 10^{-4}$, $\tau_c = 6.4 \times 10^{-5}$ and $m_e = 5.4 \times 10^{-7}$.

$$\widetilde{W}_{s0} = \frac{(s-1)g\tilde{d}^2}{18\nu}. \quad (12)$$

Hence, by specifying $\widetilde{W}_{s0} = 0.5$ mm/s (or $W_{s0} = 9 \times 10^{-4}$), these simulations can be interpreted as corresponding to fine silt (no flocculation) with a particle size of $\tilde{d} = 24\,\mu$m and the specific gravity is $s=2.65$.

As one of the objectives in this study is to evaluate the uncertainties associated with the parameterization of settling velocity adopted by the previous studies, namely, Eq. (11), simulations are designed to vary the selected parameters that stem from the baseline Case 0 (see Table 1). Case 0 is identical to a case reported in Cheng et al. (2015), which belongs to transport mode II. Specifically, the fine sediment transport of $W_{s0} = 9 \times 10^{-4}$ with a relative low dimensional critical shear stress of erosion of $\tilde{\tau}_c = 0.02$ Pa in the wave condition of $Re_\Delta = 1000$ is studied in Case 0. As reported in Cheng et al. (2015), although transport mode II is obtained for Case 0 where the flow is turbulent below the lutocline, the resulting sediment availability is in fact quite large and further reducing $\tilde{\tau}_c$ to 0.01 Pa produces laminarized transport mode III. Therefore, in this study we focus on varying the parameterizations of settling velocity and evaluate the results especially in terms of the transition of transport modes. Following Cheng et al. (2015), we also set $m_e = 5.4 \times 10^{-7}$.

For Case 0, the particle response time and characteristic flow time scale are $\tilde{t}_p = 8.5 \times 10^{-5}$ s and $\tilde{t}_l \approx 3.2 \times 10^{-3}$ s, respectively. The resulting Stokes number is $St = \tilde{t}_p/\tilde{t}_l \approx 0.03$, which is much smaller than unity. However, the non-dimensional settling velocity $W_{s0} = 9 \times 10^{-4}$ is also quite small. Hence, it is not obvious if the third term in Eq. (3), representing the inertia effect, is always smaller than the second term (Stokes settling velocity) unless flow acceleration is small. In the present boundary layer setting with gravitational acceleration acting only in the z direction, the main difference is that the second term in Eq. (3) is persistent throughout the simulation while since there is no ensemble-averaged mean flow in the z direction, the third term in Eq. (3) can only be large instantaneously. Because the system is nonlinear, it remains necessary to evaluate the importance of the third term on the resulting sediment transport at $St=0.03$ and Case A1 shown in Table 1 is presented for this purpose. To further emphasize the effect of particle inertia, two additional numerical experiments (Case A2 and A3) with higher Stokes numbers are carried out, while the other non-dimensional quantities, namely, Re_Δ, W_{s0} and Fr are kept the same as Case 0. The equilibrium Eulerian approximation is fairly accurate for $St \le 0.2$ (Balachandar and Eaton, 2010), thus the largest St is chosen to be 0.2 (Case A3).

In addition, the hindered settling effects were neglected in the previous studies (Ozdemir et al., 2010; Cheng et al., 2015). To incorporate the effect of hindered settling, the bulk settling velocity W_s is corrected with a hindered settling function $f(\phi)$:

$$W_s = W_{s0} f(\phi). \quad (13)$$

In this study, we choose the model of Richardson and Zaki (1954) to parameterize the hindered settling effect:

$$f(\phi) = \left(1 - \frac{\phi}{\phi_{ref}}\right)^m, \quad (14)$$

where ϕ_{ref} is the reference concentration, i.e., a maximum packing concentration (Richardson and Zaki, 1954; Mehta, 1986; Dankers and Winterwerp, 2007). Clearly, the degree of hindered settling and hence the resulting transport is highly dependent on ϕ_{ref}. For non-cohesive sediments, ϕ_{ref} corresponds to the maximum packing limit, which is around 0.63, at which the mean distance between the edges of the nearest neighbors is nearly zero (Berryman, 1983). For cohesive sediments, fine particles (primary particles) are transported as flocs and the gelling concentration is often used for ϕ_{ref}. As the gelling concentration is defined as the concentration at which floc aggregates form concentrated networks, it depends on the floc structures and may vary due to floc dynamics (Winterwerp, 1998; Dyer and Manning, 1999). In this study, we investigate four cases with different reference/gelling concentrations associated with non-cohesive particles (see Case B1 in Table 1), and different floc structures (Cases B2–B4 in Table 1). The empirical exponent m is related to the particle Reynolds number ($Re_p = \widetilde{W}_{s0}\tilde{d}/\nu$). As will be demonstrated later, the particle size (or floc size) considered in this study is small ($Re_p < 0.2$) and the exponent m is kept constant as $m=4.6$ (Richardson and Zaki, 1954).

3. Effect of particle inertia

To study the effect of particle inertia, four numerical experiments are carried out and results are compared in non-dimensional quantities. In Case 0 (see Table 1), the inertia terms in the sediment velocity expression are neglected and Eq. (11) is used. In Cases A1–A3 (see Table 1), the first-order inertia term in the sediment velocity expression is kept:

$$u_i^s = u_i - W_{s0}\delta_{i3} - St\left(1 - \frac{1}{s}\right)\frac{Du_i}{Dt}. \quad (15)$$

Except for the difference in the particle velocity expressions, other non-dimensional flow and sediment parameters in Case 0 and Case A1–A3 are kept the same, and thus any difference between these cases is due to the extra inertia term in the particle velocity expression.

3.1. Model results

The sensitivity of the particle inertia is first investigated by comparing the ensemble-averaged profiles (see Fig. 3) of sediment concentration, non-dimensional streamwise velocity and non-dimensional turbulence intensity for Case 0 (inertia effect neglected) and Case A1 ($St=0.03$). The turbulence intensity is defined as $\langle\sqrt{2k}\rangle$, where '$\langle\ \rangle$' denotes the averaging operation over the $x-y$ plane, and k is the turbulent kinetic energy:

$$k = \frac{1}{2}(u'^2 + v'^2 + w'^2), \quad (16)$$

where u', v' and w' are the velocity fluctuations of streamwise, spanwise and vertical velocity components, respectively.

It is reminded here that Case 0 belongs to transport mode II, in which the lutocline separates the upper quasi-laminar layer from the lower turbulent layer. In this case, the lutocline is located approximately at $z = 13$–14 (see circle symbols in Fig. 3(a)). By including the first-order inertia term, the resulting sediment concentration profile (see Fig. 3(a)) is very similar to that of Case 0. Moreover, the relative difference of the sediment concentration is shown in Fig. 3(d), which is defined as

$$\mathrm{Err}(\langle\phi\rangle) = \frac{\langle\phi_A\rangle - \langle\phi_0\rangle}{\langle\phi_0\rangle} \times 100\%, \quad (17)$$

where $\langle\phi_0\rangle$ is the plane-averaged sediment concentration in Case 0, and $\langle\phi_A\rangle$ is the plane-averaged sediment concentration in Case A1. The relative difference of the streamwise velocity $\mathrm{Err}(\langle u\rangle)$ and the turbulent intensity $\mathrm{Err}(\langle\sqrt{2k}\rangle)$ can be calculated in a similar manner. We can see that the overall relative difference is small (<10%). A reduction of sediment concentration can be observed in the range of $13 < z < 21$, and the peak difference appears at

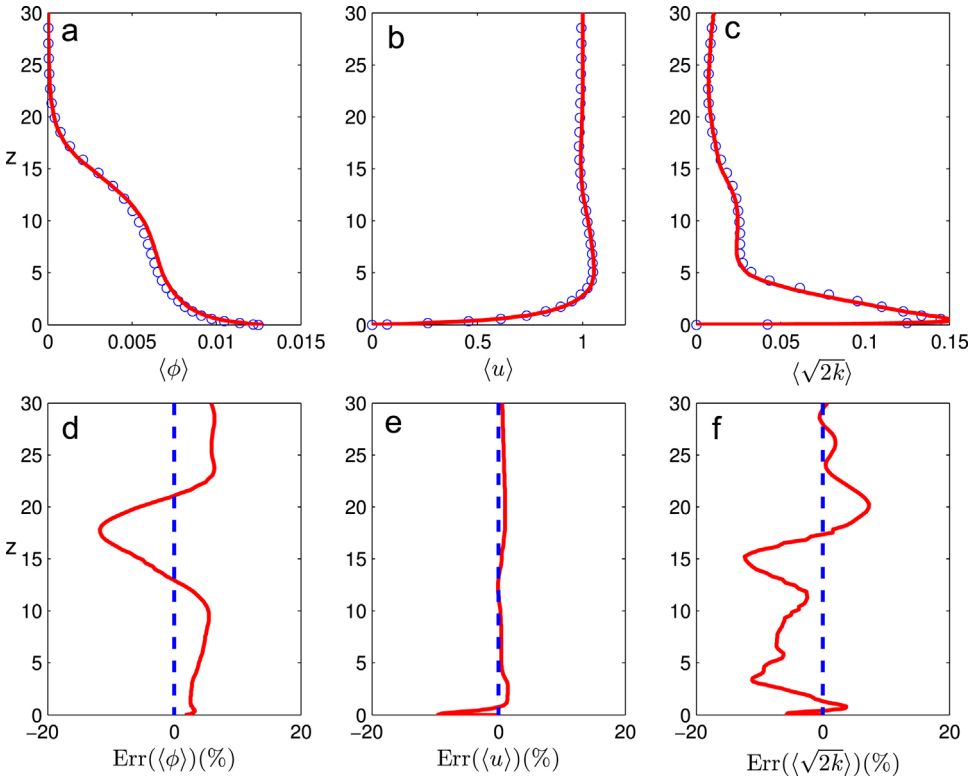

Fig. 3. Comparison of the ensemble-averaged profiles of (a) sediment concentration, (b) streamwise velocity and (c) turbulence intensity during flow peak ($\omega t=0$) for Case 0 (circle symbols), Case A1 (solid curve). The relative difference (%) of these flow quantities are shown in (d), (e) and (f), respectively. The levels of zero error are denoted as dashed lines in (d), (e) and (f).

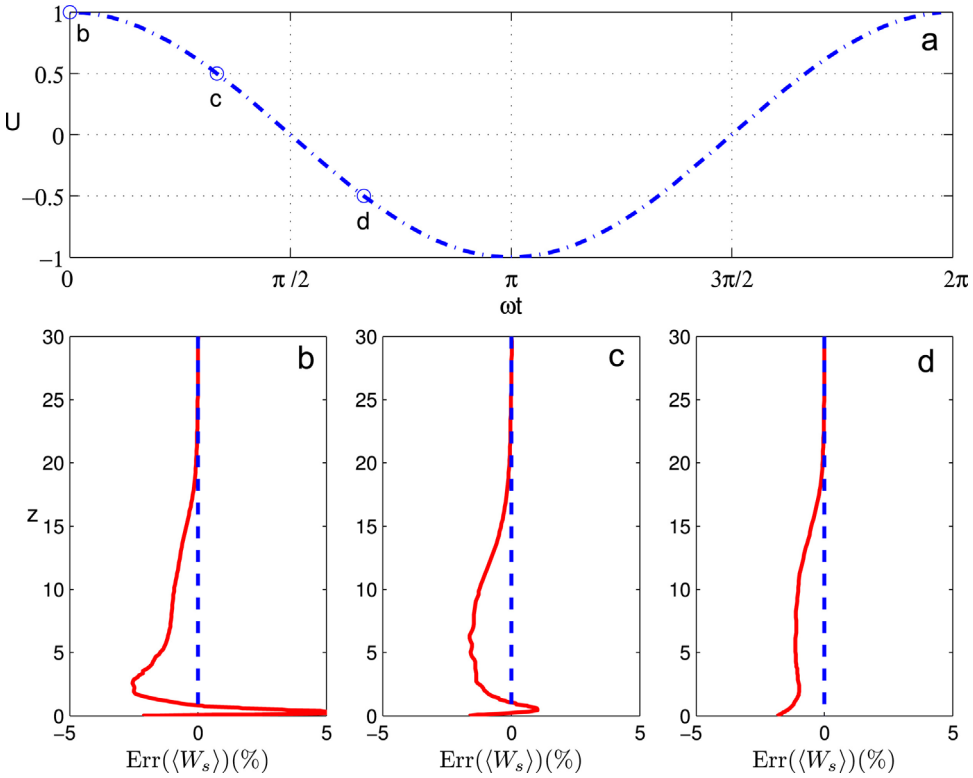

Fig. 4. (a) Time series of free-stream velocity $U(t)$. Three representative instants (b, c, d) are shown with open circles. The relative difference (%, solid curve) of effective settling velocities between Case 0 and Case A1 at these three representative instants are shown in (b) flow peak ($\omega t=0$), (c) $\omega t = \pi/3$ and (d) $\omega t = 2\pi/3$; The levels of zero error are denoted as dashed lines in (b), (c) and (d).

around $z=18$ (about -10%), which is close to the lutocline. On the contrary, sediment concentration below $z=13$ is increased by about 7%. This observation suggests the lowering of lutocline when inertia effect is considered. Meanwhile, the streamwise velocities (see Fig. 3(b)) of both cases are again very similar, and the relative difference (see Fig. 3(e)) is generally smaller than 5%, and the peak value can be observed near the bottom. Furthermore, the comparison of turbulence intensity is shown in Fig. 3(c). Although the turbulence intensity profiles from Case 0 and Case A1 are also very close, it is evident that the predicted turbulence is slightly lower by including the inertia effect with the peak attenuation which occurs at around $z=15$ near the lutocline. More attenuated turbulence is consistent with the lowered lutocline.

Moreover, the relative differences in effective settling velocities at three representative instants are discussed in Fig. 4. The relative difference in the effective settling velocity is calculated by the ensemble-average of the additional term associated with the inertia effect normalized by W_{s0}:

$$\mathrm{Err}(\langle W_s\rangle) = St\,(1-\frac{1}{s})\frac{\left\langle \frac{Dw}{Dt}\right\rangle}{W_{s0}}\times 100\% \tag{18}$$

In Fig. 4(a), the wave phase (ωt) is defined such that $\omega t=0$ ($\omega t=\pi$) corresponds to the positive (negative) peak of free-stream velocity, and $\omega t=\pi/2$ and $3\pi/2$ correspond to flow reversals. From the comparison of effective settling velocities (Fig. 4(b–d)), we can see that the effective settling velocity is nearly unaffected above $z=20$ due to very low turbulence above the lutocline. Between $1.5<z<20$, including the particle inertia reduces the effective settling velocity. However, the reduction is only within 3%. Moreover, an increase of the effective settling velocity can be observed near the bottom $0<z<1.5$, and the peak value of the increment is about 5% at flow peak. However, the effective settling velocity at the bottom is still reduced by about 2%. As the flow decelerates to $\omega t=\pi/3$, the increment of effective settling velocity at around $z=1.5$ is decreased to about 1%. After the flow reserves and accelerates to $\omega t=2\pi/3$, a uniform reduction of effective settling velocity can be observed below the lutocline, and the reduction is less than 2%. Overall, the inertia effect slightly reduces velocity fluctuations in the z-direction and hence the Reynolds stress is reduced (not shown here for conciseness). This can further lead to a reduction of turbulent production and hence more attenuation of turbulence. However, the Stokes number considered here remains to be too small ($St=0.03$) to trigger the transition to transport mode III.

As discussed in this section, by retaining the first order St term in the particle velocity expansion based on Case 0 with $St=0.03$, the inertia effect is demonstrated to be small on concentration profiles, velocity profiles and turbulent intensity. This negligible effect is consistent with the small $\mathrm{Err}(\langle W_s\rangle)$ which is generally within 5%. This sensitivity study of inertia effect justifies the previous studies where the inertia terms are neglected. Simulation results for Case A2 and A3 demonstrating more pronounced evidence that particle inertia effect can attenuate turbulence are presented in Discussion (Section 5.1).

4. Effect of Hindered settling

Ozdemir et al. (2011) have demonstrated that the settling velocity plays a key role in determining the vertical sediment flux budget, and vertical distribution of sediment concentration. Meanwhile, it has been shown that the settling velocity directly affects the deposition flux at the bottom, and therefore determines the sediment availability (Cheng et al., 2015). Both sediment availability and vertical structure of sediment concentration have significant impacts on the carrier flow turbulence characteristics via stable density stratification. Therefore, it is intrinsic to study the effect of hindered settling on fine sediment transport. As demonstrated in Section 3, the particle inertia has negligible effects on the fine sediment transport for Stokes number St up to 0.03. Therefore, in the study of hindered settling effects, the inertia effect is neglected. Neglecting the inertia effect in particle velocity parameterization also allows us to easily isolate the hindered settling effect. In this section, the particle velocity is expressed to account for the hindered settling correction:

$$u_i^s = u_i - W_{s0} f(\phi)\delta_{i3}. \tag{19}$$

When fine sediments are considered non-cohesive, the reference concentration is chosen to be $\phi_{ref}=0.63$, which corresponds to Case B1 in Table 1, and the dimensional Stokes settling velocity $\widetilde{W}_{s0}$ is calculated by Eq. (12). Hence, for Case 0 and Case B1, a dimensional settling velocity of $\widetilde{W}_{s0}=0.5$ mm/s corresponds to fine silt of grain diameter $\tilde{d}=24\,\mu$m. For cohesive sediments forming floc aggregates, the dimensional Stokes settling velocity should be determined by floc properties (Kranenburg, 1994):

$$\widetilde{W}_{s0} = \frac{(s^{floc}-1)g\widetilde{D}_f^2}{18\nu}, \tag{20}$$

where $\widetilde{D}_f$ is the floc size, and $s^{floc}=\rho^{floc}/\rho^f$ is the specific gravity of flocs with ρ^{floc} being the density of flocs. The floc density depends on floc structures, and it is calculated by adopting the fractal model (Kranenburg, 1994) as

$$\rho^{floc} = \rho^f + (\rho^s-\rho^f)\left(\frac{\widetilde{D}_f}{\tilde{d}}\right)^{(n_f-3)}, \tag{21}$$

where n_f is the fractal dimension and $\tilde{d}$ is interpreted here as the primary particle size. For flocs, the gelling concentration is used as the reference concentration (see Eq. (14)). The gelling concentration is also determined by floc structures, which is calculated as (e.g., Winterwerp and Van Kesteren, 2004)

$$\phi_{gel} = \left(\frac{\widetilde{D}_f}{\tilde{d}}\right)^{n_f-3} = \frac{\rho^{floc}-\rho^f}{\rho^s-\rho^f}. \tag{22}$$

Due to complicated processes of floc aggregation and breakup, floc properties may vary with flow shear and floc–floc interactions (Dyer and Manning, 1999; Winterwerp, 1998). However, this level of complexity is beyond the scope of this study, and floc properties are assumed to be constant in each simulation. We consider the primary particle size to be $\tilde{d}=4\,\mu$m, the floc size $\widetilde{D}_f$ and fractal dimension n_f are then determined by keeping the Stokes settling velocity the same as Case 0, i.e., $\widetilde{W}_{s0}=0.5$ mm/s (or $W_{s0}=9\times10^{-4}$). For example, in Case B2 we specify the gelling concentration to be $\phi_{gel}=0.2$. Matching the Stokes settling velocity of $\widetilde{W}_{s0}=0.5$ mm/s gives a floc size of $\widetilde{D}_f=53.7\,\mu$m with the fractal dimension $n_f=2.38$. This corresponds to typical inorganic flocs with n_f significantly greater than 2.0. On the other hand, Case B4 with a gelling concentration of $\phi_{gel}=0.05$ gives a floc size of $\widetilde{D}_f=107\,\mu$m and $n_f=2.09$, which corresponds to more porous and organic flocs. The floc properties for all the cases considered in this study are summarized in Table 1. We can check that the maximum particle Reynolds number considered in Table 1 remains to be very small $Re_p=0.06$. Thus, a constant $m=4.6$ (see Eq. (14)) can be used in all the cases.

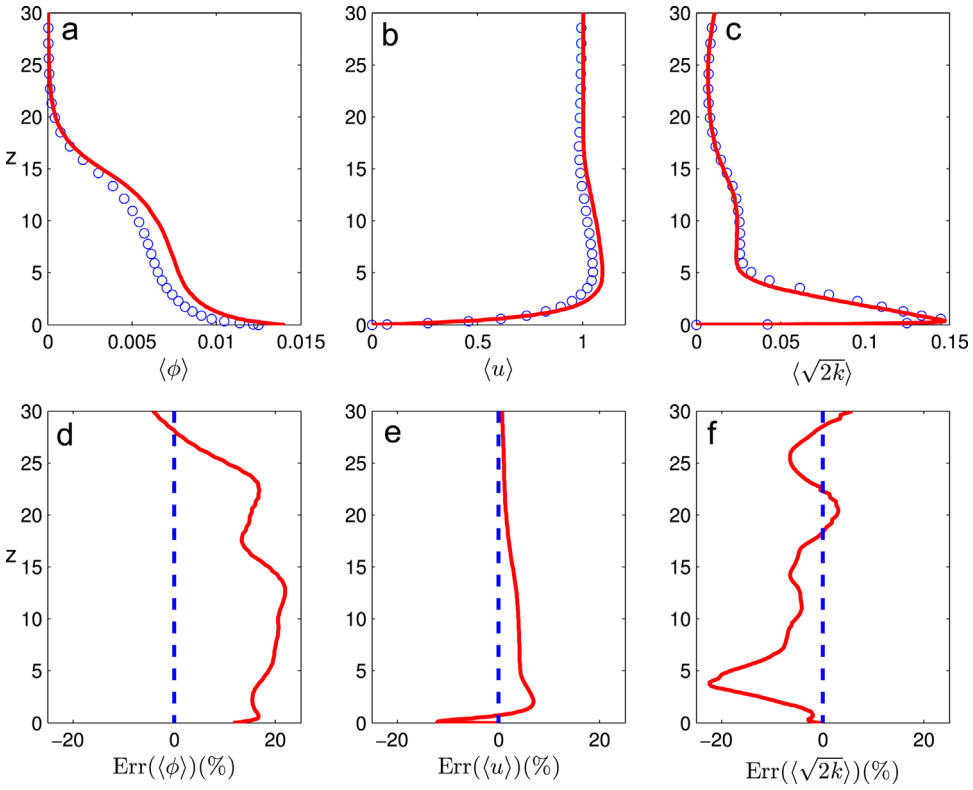

Fig. 5. Comparison of the ensemble-averaged profiles of (a) sediment concentration, (b) streamwise velocity and (c) turbulence intensity during flow the peak ($\omega t=0$) for Case 0 (circle symbol), Case B1 (solid curve). The relative difference (%) of these flow quantities are shown in (d), (e) and (f), respectively. The levels of zero error are denoted as dashed lines in (d), (e) and (f).

4.1. Model results

Using the model of Cheng et al. (2015), the sediment availability in this study is determined by the interplay of erosion and deposition at the bottom boundary. However, the hindered settling adds another layer of complexity, since the settling velocity becomes a function of sediment concentration (see Eq. (13)) and the deposition flux is now a nonlinear function of sediment concentration. Hence, it is crucial to study the uncertainty introduced by hindered settling on the transport mode of fine sediment.

Firstly, the ensemble-averaged flow statistics in Case 0 and Case B1 are compared in Fig. 5 to study the sensitivity of the hindered settling for non-flocculated condition (ϕ_{ref} = 0.63). Case 0 and Case B1 show a similar feature of concentration profiles (Fig. 5(a)). Since the lutoclines are observed in both Case 0 and Case B1 near $z=14$, transport mode II is also obtained for Case B1. However, Case B1 shows slightly increased sediment concentrations below the lutocline. Although the increase is within 20%, this notable increment of total load in the domain is clearly associated with the reduced settling velocity through hindered settling. Meanwhile, the streamwise velocity profiles (see Fig. 5(b)) show that the overshoot near the bottom in Case B1 is slightly larger (within 10%) than that of Case 0. Below the lutocline, the turbulent intensity in Case B1 is consistently lower than that of Case 0 by about 5–20% (see Fig. 5(f)). When settling velocity is effectively reduced by hindered settling effect, more sediments are suspended in the domain (Cheng et al., 2015), which leads to an enhanced sediment-induced density stratification and a stronger attenuation of turbulence is observed. However, both Case 0 and Case B1 are in transport mode II, which verifies the simulations of Cheng et al. (2015), where the hindered settling effect is neglected as sediments are assumed to be non-flocculated.

Though the transport mode is not altered, a noticeable damping effect of flow turbulence is observed when the hindered settling is considered. It is motivated to further investigate the hindered settling effect with different reference (gelling) concentrations (see Cases B2-B4 with different gelling concentration shown in Table 1). As a result of different gelling concentrations, distinct transport modes are observed. These distinct transport modes are first examined from the ensemble-averaged flow statistics for Case B1 and B2. Fig. 6 illustrates the hindered settling effect on the vertical structure of sediment concentration, streamwise velocity and turbulent intensity. As discussed before, transport mode II with a lutocline is observed for Case B1 (see solid curves in Fig. 6 (a) and (d)). By reducing the reference (gelling) concentration from ϕ_{ref} = 0.63 to ϕ_{ref} = 0.2, Case B2 (see dashed curve in Fig. 6 (a) and (d)) shows a very different feature of sediment concentration. The lutocline is not observed in the concentration profile of Case B2, and nearly exponential profile is obtained. From the velocity profiles shown in Fig. 6(b) and (e), a reduction of bottom boundary layer thickness is also observed. More importantly, the turbulent intensity below $z=14$ is completely suppressed in Case B2, which indicates that the flow turbulence is completely attenuated by sediment-induced stable density stratification. Above $z=14$, a weak turbulent intensity can still be observed, and this is introduced by the turbulent fluctuation from the upper wall. During the flow reversal, significantly attenuated turbulence (or laminar-like features) is also obtained for Case B2. From the flow statistics, we observe that Case B1 is in transport mode II, while further reducing the reference (gelling) concentration associated with hindered settling triggers the transition from transport mode II to laminarized transport mode III.

To further illustrate the effect of hindered settling on the turbulent structure and the resulting turbulence-sediment

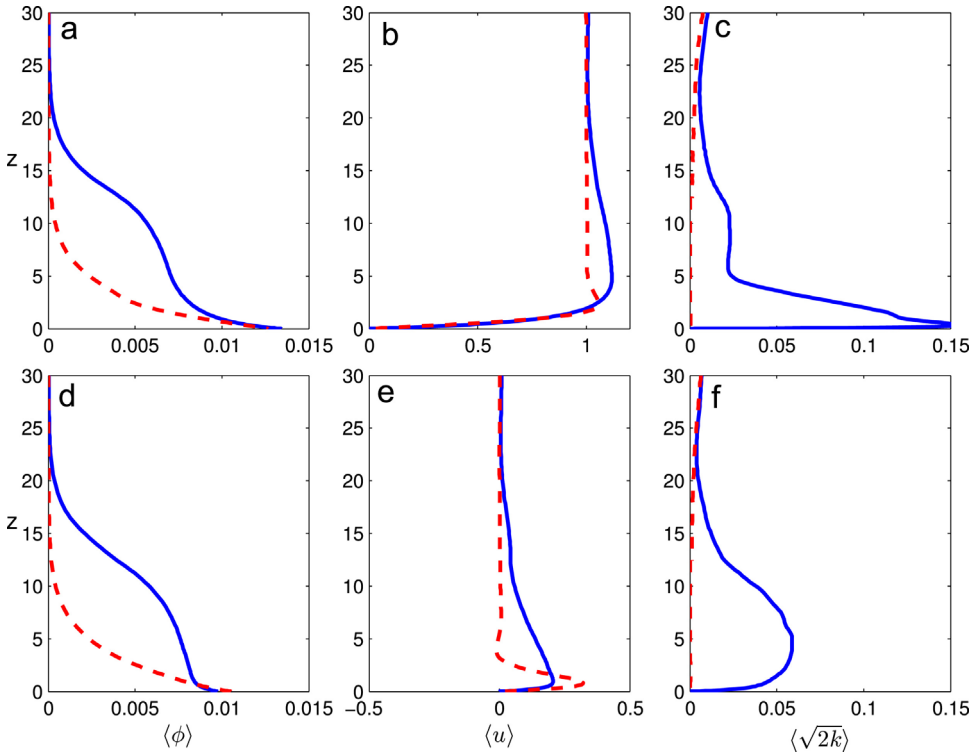

Fig. 6. Ensemble-averaged profiles of (a) sediment concentration, (b) streamwise velocity and (c) turbulent intensity during flow peak ($\omega t=0$) for Case B1 (solid curve), Case B2 (dashed curve). (d), (e) and (f) are the corresponding profiles during flow reversal.

interaction, the iso-surfaces of local swirling strength λ_{ci} are shown along with the iso-surface of sediment concentration for Case 0, B1 and B2 during the flow peak in Fig. 7. λ_{ci} is the imaginary part of the complex eigenvalue of the velocity gradient tensor and its magnitude can be used to quantify the strength of local swirling motion (Zhou et al., 1999). The threshold is chosen here to be 4% of the maximum value obtained in Case 0, and this threshold value is applied to the other cases to facilitate the comparison. It is evident that sparse coherent vortex structures can be observed in part of the near-bed region in Case 0 (see Fig. 7 (a)). This region is corresponding to a stripe of more irregular/chaotic and higher sediment concentration structures. In regions where no coherent turbulence structures are observed, a regularly spaced streaks of lower sediment concentration are observed. When hindered settling is considered with reference concentration ϕ_{ref} = 0.63 (see Case B1 in Fig. 7(b)), similar sparse coherent vortex structures can be seen but with slightly sparser distribution than that in Case 0. On the other hand, no coherent vortex structures can be observed in Case B2 (see Fig. 7(c)), which indicates that the turbulence in Case B2 is completely suppressed. As a result, a nearly uniform sediment concentration structures appears in the sediment concentration field of Case B2. Although not shown here, further reducing the reference concentration to ϕ_{ref} = 0.13 (Case B3) and ϕ_{ref} = 0.05 (Case B4) also shifts the flow to laminarized transport mode III, and the flow turbulence structures for Case B3 and Case B4 are similar to Case B2.

These distinct flow features are caused by different degrees of hindered settling effect. Fig. 8 presents the normalized effective settling velocity, which is defined as the difference between the sediment velocity and the fluid velocity in the z-direction normalized by the Stokes settling velocity. Since the features are similar during the entire wave cycle, only the comparison at the flow peak is shown here. We can see that different reference (gelling) concentrations render different degrees of reduction in the effective settling velocity, and the reduction of effective settling velocity is larger near the bottom, where the sediment concentration is larger. For Case B1 (ϕ_{ref} = 0.63), the reduction is less than 10%. When the reference concentration ϕ_{ref} is reduced to 0.2 (or 0.13) in Case B2 (in Case B3), the reduction of settling velocity is significantly enhanced and near the bed, the effective settling is only 60% (37%) of that in Case 0. Finally, the complete hindered effect, where the effective settling velocity approaches zero near the bottom is observed for reference concentration ϕ_{ref} = 0.05 (Case B4).

It has been revealed that settling velocities play an important role in vertical structure of sediment-induced density stratification (Ozdemir et al., 2011) and sediment availability (Cheng et al., 2015), which determines the flow transport modes. Fig. 9 (a) further illustrates the hindered settling effect on the time series of domain-averaged sediment concentration, which is defined as

$$\Phi = \frac{1}{L_z}\int_0^{L_z} \langle\phi\rangle\, dz. \tag{23}$$

It is evident from Fig. 9(a) that Φ is significantly affected by the hindered settling. For non-flocculated condition (Case B1, ϕ_{ref}=0.63), the temporal variation of domain-averaged sediment concentration is similar to that of Case 0. An equilibrium state in transport mode II is established, in which the wave-averaged erosion flux $\overline{E}$ balances the wave-averaged deposition flux $\overline{D}$ with '$\overline{\ }$' representing wave-averaged operator. The deposition flux at the bottom boundary is determined by the bottom concentration, which plays a key role in controlling the sediment availability in the domain. Therefore, the evolution of the ensemble-averaged bottom concentration $\langle\phi_b\rangle$ is also presented in Fig. 9(b). For both Case 0 and Case B1, time series of $\langle\phi_b\rangle$ are similar to that of Φ and an equilibrium state is achieved after about 20 repeated wave motions. To facilitate the comparison, we also examine the time averaged Φ over one wave period at the equilibrium stage and

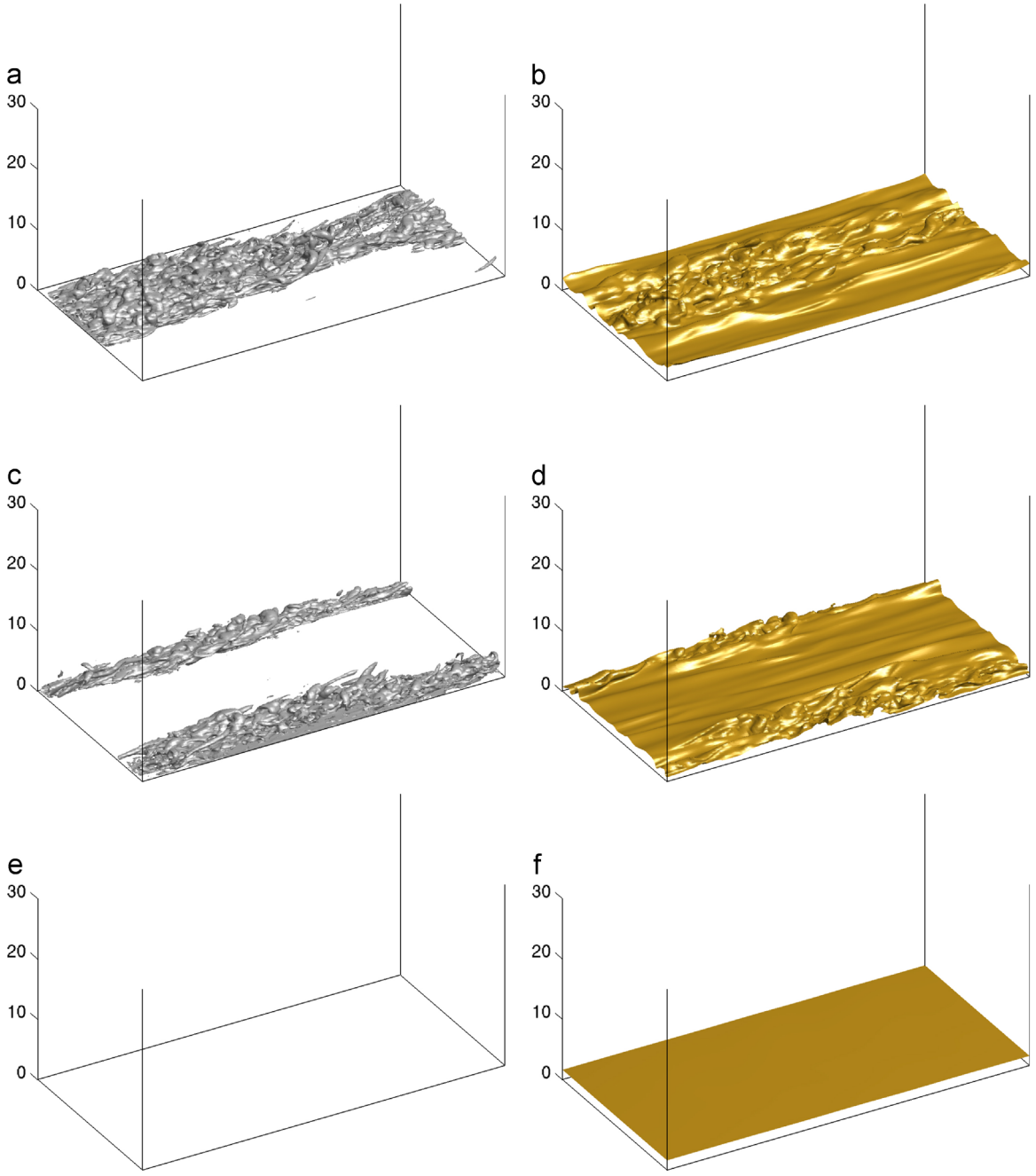

Fig. 7. Turbulent coherent structures at flow peak ($\omega t=0$) for (a) Case0, (c) Case B1, and (e) Case B2. The turbulent coherent structures are visualized using the swirling strength (λ_{ci}), and the contour level used here is 4% of the maximum λ_{ci} value in Case 0. The iso-surface of concentration ϕ field corresponding to (b) Case 0, (d) Case B1 and (f) Case B2 are also shown, and their contour levels are 8.2×10^{-3}, 9.8×10^{-3} and 0.015, respectively.

formally define it as sediment availability $\overline{\Phi}_{eq}$ (see Table 1). The sediment availability for Case B1 ($\overline{\Phi}_{eq} = 1.95 \times 10^{-3}$) is slightly greater than that of Case 0 ($\overline{\Phi}_{eq} = 1.76 \times 10^{-3}$), which is consistent with the slightly lower settling velocity in Case B1. This equilibrium state reflects transport mode II and the turbulent nature of this mode sustain a notable amount of sediment (see Table 1).

However, when the gelling concentration is further reduced to $\phi_{ref} = 0.2$ and $\phi_{ref} = 0.13$, a different trend of sediment concentration evolution can be observed. The domain-averaged sediment concentration Φ increases to about 2.1×10^{-3} (2.4×10^{-3}) in Case B2 (Case B3) at $t/T = 10$ ($t/T = 12$). Afterward, Φ starts to decrease. As discussed previously (see Figs. 6 and 7(c)), the flow turbulence in Case B2 (or Case B3) is completely suppressed (laminarized transport mode III) and the viscous suspension alone can not sustain such amount of sediment in the domain. As a result, the domain-averaged concentration drops until a final equilibrium state in the laminarized transport mode III is reached and a much lower $\overline{\Phi}_{eq}$ is found. Notice that the decreasing rate of domain-averaged sediment concentration in Case B3 is smaller than that in Case B2, and this difference can be explained by the different effective settling velocities as shown in Fig. 8.

More insights can be revealed by examining the time series of bottom concentration $\langle \phi_b \rangle$. In in Fig. 9(b), $\langle \phi_b \rangle$ of Case B2 increases slightly faster than that of Case B1 (compare the blue curve with the red curve). Similar features in the bottom concentrations are

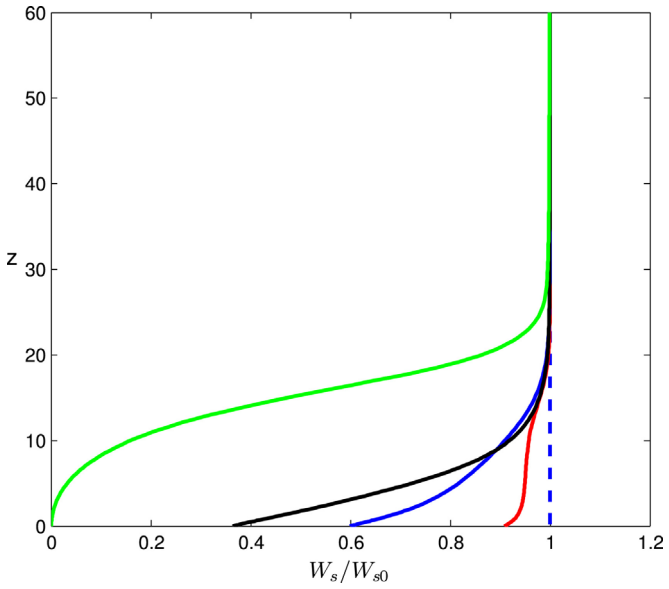

Fig. 8. Normalized effective settling velocity profile for Case 0 (dashed curve), Case B1 (circle symbols), Case B2 (curve with cross symbols), Case B3 (dash-dot curve) and Case B4 (thick solid curve) during flow peak (t=15 T).

also observed for Case B3 (black curve in Fig. 9(b)). This sharper increase of bottom concentration is clearly associated with the collapse of flow turbulence at around t=13 T for Case B2 (or t=10 T for Case B3), and hence a larger increment rate of the bottom concentration must then occur for the next couple of wave cycles. This process is more clearly demonstrated in Fig. 10(a) and (b). Before the flow laminarizes (t < 13 T), the flow is evidently turbulent with peak turbulent intensity exceeding 0.15 (see Fig. 10 (b)), and a lutocline is observed from the corresponding concentration profiles. At t=13 T, the turbulent intensity drops significantly and the peak value is of no more than 0.04. Two more wave periods later at t=15 T, the turbulent intensity is almost vanished. To respond to the suppression of turbulence, sediment concentrations in the range of 5 < z < 20 is reduced. Meanwhile, an accumulation of sediment concentration near the bottom (z < 5) is observed. The increased sediment concentration near the bed can further reduce the effective settling velocity (see Eq. (14)), however the deposition rate is increased (demonstrated later in Fig. 13), thus the bottom concentration then generally drops until the final equilibrium state is reached (see Fig. 9(b)). The interplay between the deposition flux and bottom concentration after laminarization further determines the equilibrium balance between erosion flux and deposition flux. Quantitatively, the erosion flux after laminarization in the numerical simulation is only determined by viscous suspension, which is sensitive to the Schmidt number *Sc* specified. However, the qualitative feature discussed here is unaffected by the value used for *Sc*.

From the above discussions, we can clearly observe that significantly suppressed turbulence and laminarized transport mode III is obtained for Cases B2 and B3 due to initially high sediment availability, which is consistent with the finding discussed in Cheng et al. (2015). However, in Cheng et al. (2015), the high sediment availability is obtained via a lower critical shear stress of erosion (lower than the value used here), while in this study, the higher sediment availability is associated with a significant hindered settling effect. Indeed, Cheng et al. (2015) also demonstrated that by systematically reducing the settling velocity used in each simulation, larger availability is obtained which can also lead to laminarization.

If we further reduce the reference concentration as in Case B4 (ϕ_{ref} = 0.05), we would expect laminarized transport mode III with even lower sediment availability $\overline{\Phi}_{eq}$ than that in Case B3. However, the time series of domain-averaged concentration shows unexpected features. We can observe that the domain-averaged concentration continue to increase as wave motion persists. Eventually the increment rate becomes relatively constant, however, an equilibrium state such as those of Cases B1–B3 cannot be established. This unbounded mode of suspended sediment load in the domain is caused by the significantly reduced deposition flux

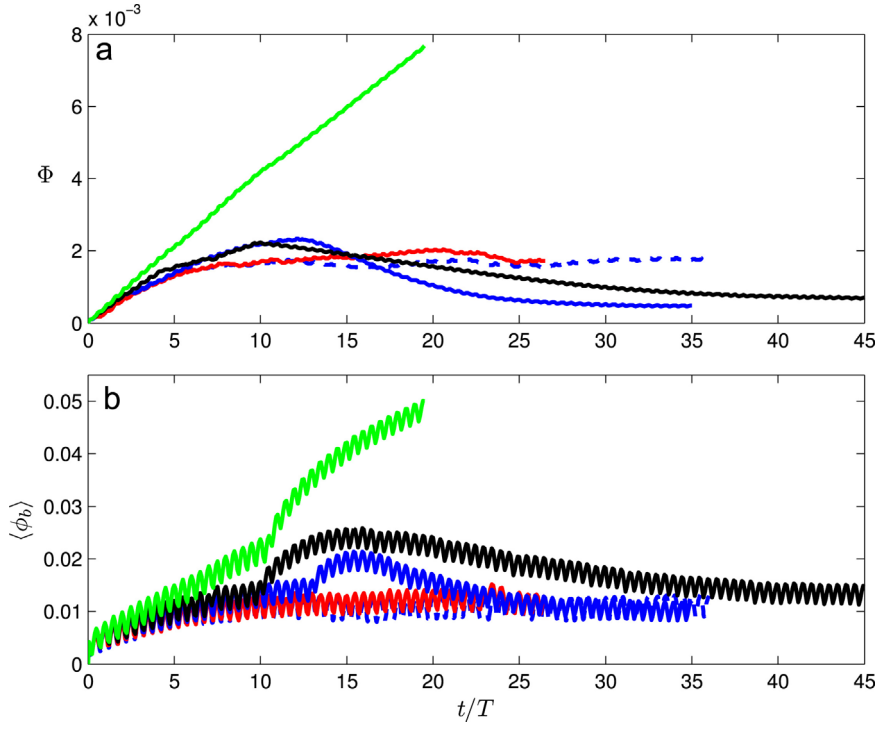

Fig. 9. Temporal evolution of (a) domain-averaged sediment concentration Φ and (b) ensemble-averaged sediment concentration at the bottom $\langle\phi_b\rangle$ for Case 0 (thin solid curve), Case B1 (circle symbols), Case B2 (curve with cross symbols), Case B3 (dash-dot curve) and Case B4 (thick solid curve).

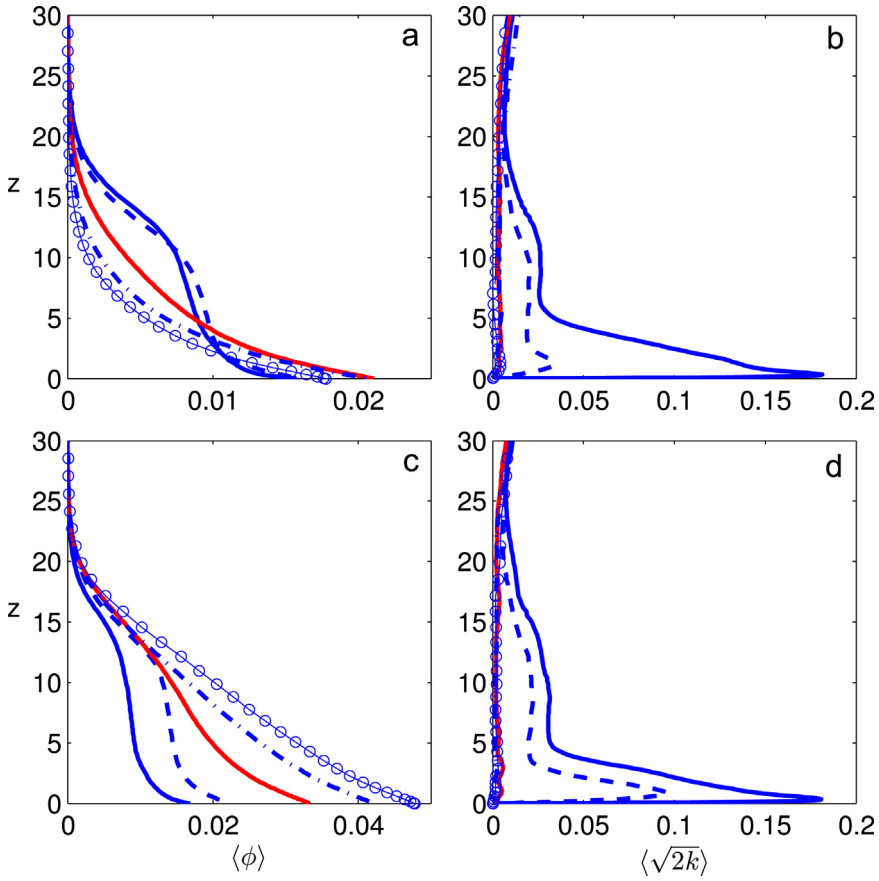

Fig. 10. Plane-averaged (a) sediment concentration profiles and (b) turbulent intensity profiles for Case B2 at five different instants: $t=11$ T (solid curve), $t=13$ T (dashed curve), $t=15$ T (curve with cross symbols), $t=17$ T (dash-dot curve), $t=19$ T (curve with circle symbols). The corresponding plane-averaged profiles for Case B4 are shown in (c) and (d) at five different instants: $t=6$ T (solid curve), $t=9$ T (dashed curve), $t=12$ T (curve with cross symbols), $t=15$ T (dash-dot curve), $t=18$ T (curve with circle symbols).

(or nearly zero deposition flux) associated with very large hindered settling effect.

According to the time series of bottom concentration of Case B4 shown in Fig. 9(b), the larger increment rate after the laminarization at $t=10$ T is consistent with that of Cases B2 and B3. However, the subsequent time series of $\langle\phi_b\rangle$ of Case B4 again shows a trend of continue increment, which indicates that the equilibrium balance between the erosion flux and the deposition flux cannot be established. From the snapshots of sediment concentration and turbulent intensity profiles (see Fig. 10(c) and (d)), during the early stage of the simulation at $t=6$ T (or $t=9$ T), a lutocline can be observed in the concentration profile and the flow is turbulent. After the onset of laminarization, the flow turbulence is almost completely suppressed (see $t=12$ T) and the sediment concentration shows the expected concave-upward profile. What is unexpected is that by comparing the concentration profile between $t=15$ T and $t=18$ T, it becomes clear that the total amount of suspended sediment in the domain (or sediment availability) continues to increase cycle by cycle. Hence, by considering the hindered settling with a very low gelling concentration, the flow feature obtained in Case B4 after the onset of laminarization is distinctly different from that of Cases B2 and B3. The flow feature demonstrated in Case B4 is similar to the gelling ignition discussed in Kampf and Myrow (2014). It is reminded that when the sediment concentration becomes large, the assumptions of the equilibrium Eulerian approximation and Boussinesq approximation may be violated. To confirm this, the maximum concentrations ϕ_{max} in each case are also shown in Table 1. We can see that the maximum concentration in each is no more than 0.05, which is sufficiently small. In Case B4, the simulation is terminated as the bottom concentration exceeds 0.05, however, the fate of the sediment transport at this point is already clear.

In summary, the transition from transport mode II to transport mode III can be triggered by the hindered settling with a low reference (gelling) concentration. This transition of transport modes is due to the reduction in the effective settling velocity when the hindered settling is considered. As discussed in Cheng et al. (2015), the reduced settling velocity can increase the sediment availability, and the resulting sediment-induced stable density stratification is enhanced that further triggers the flow laminarization. Interestingly, in the laminarized transport mode III, an unstable mode, where the deposition flux becomes always smaller than the erosion flux, is obtained when a sufficiently low gelling concentration is used. In the next section, we will show that the observed unstable mode is indeed the gelling ignition as described in Kampf and Myrow (2014) and a sufficient condition for its occurrence is proposed.

5. Discussion

5.1. Turbulence modulation due to increasing St

Although including the inertia terms in the particle velocity expression for fine sediment in typical continental shelf condition ($St=0.03$) makes no more than %10 difference on the mean quantities (see Fig. 3), it is likely that the inertia effect can be more pronounced when the Stokes number St is larger in Cases A2 and A3 (see Table 1). We like to also point out that Cases A2 and A3 are numerical experiments with increased Stokes number, while other

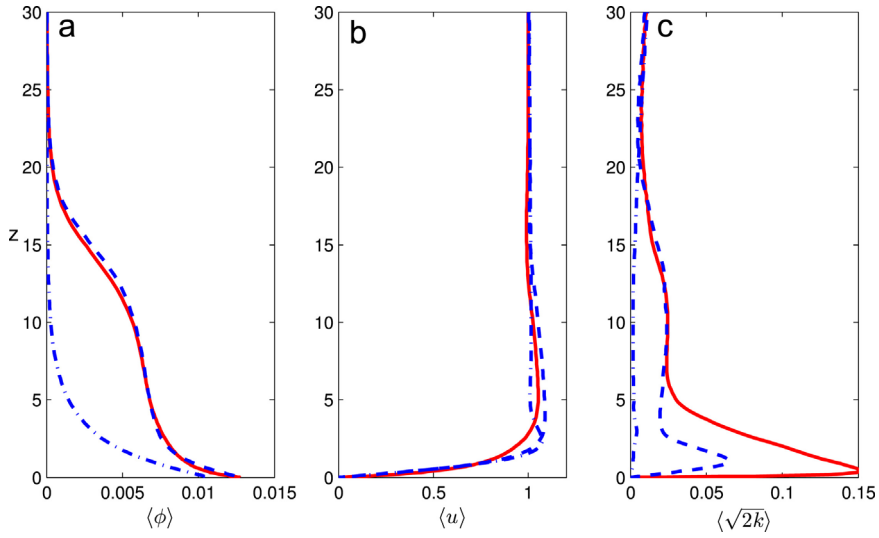

Fig. 11. Comparisons of (a) sediment concentration, (b) streamwise velocity and (c) turbulence intensity for Case A1 (solid curve), Case A2 (dashed curve) and Case A3 (dash-dot curve).

non-dimensional parameters are kept the same. Since the physical condition of Cases A2 and A3 may not occur for typical fine sediment in the continental shelf, we focus on comparing non-dimensional quantities and turbulence modulation.

Ensemble-averaged sediment concentration, fluid streamwise velocity and turbulent intensity are compared in Fig. 11 for cases with different Stokes numbers (Case A1–A3). From the concentration profiles (Fig. 11(a)), we can see that the lutoclines, which is typical for transport mode II, appear in both Cases A1 and A2. However, the lutocline is absent in Case A3, and a rapid decaying sediment concentration is observed. The boundary layer thickness is significantly reduced in Case A3, which is evident in the streamwise velocity profiles (Fig. 11(b)). Meanwhile, from the turbulence intensity profile, we observe that increasing the Stokes number, the flow turbulence is evidently decreased. Particularly, for Case A3 with $St=0.2$, the flow turbulence is almost completely suppressed. By increasing the St to about 0.2, laminarized mode III is obtained.

Previous studies found that intense and persistent local vortical structures can influence the local particle concentration field, and the effect of large particle inertia would bias the particle trajectory towards regions of high strain rate and low vorticity due to the centrifugal effect. This biased distribution of inertia particles has been identified as preferential accumulation (e.g., Wang and Maxey, 1993). If we take the divergence of the particle velocity shown in Eq. (15), due to the incompressibility of the carrier flow, the following relationship is obtained:

$$\frac{\partial u_i^s}{\partial x_i} = St\left(1-\frac{1}{s}\right)\left(\|\boldsymbol{\Omega}\|^2 - \|\boldsymbol{S}\|^2\right) = 2\,St\left(1-\frac{1}{s}\right)Q, \tag{24}$$

where $\|\boldsymbol{S}\|$ is the magnitude of strain-rate tensor, and $\|\boldsymbol{\Omega}\|$ is the magnitude of rotation-rate tensor. In an incompressible flow, the second invariant $Q = 1/2(\|\boldsymbol{\Omega}\|^2 - \|\boldsymbol{S}\|^2)$ is a local measure of the excess rotation rate relative to the strain rate (Chakraborty et al., 2005). When $s > 1$, i.e., particles are denser than the carrier fluid, the divergence of particle velocity has the same sign as Q, indicating that the particles tend to accumulate in regions where the strain rate is larger than the rotation rate (i.e. $\|\boldsymbol{S}\|^2 > \|\boldsymbol{\Omega}\|^2$). Meanwhile, it is noted that the effect of particle inertia grows as the particle Stokes number increases, which is evident from Eq. (24).

To identify the preferential concentration phenomenon, the iso-surface of the second invariant Q field is plotted against the plane cut ($z=1.5$) of the sediment concentration field at $t=10$ T for Cases 0 and A3 (see Fig. 12). At the moment of $t=10$ T presented here, both cases are still turbulent. As discussed before, denser-than-fluid inertial particles prefer to concentrate in regions of low vorticity and high strain rate. Hence, we expect that regions with negative Q values would correspond to high concentration fields. From Fig. 12(a), we can see that when inertia terms are ignored in the sediment velocity (Eq. (15)), the turbulence structures represented by negative Q value typically cover both high and low concentration regions (see the sub-panels in (a) for enlarged view). However, when the inertia terms are included with high St (see Fig. 12(b)), the high correlation between turbulence structures represented by negative Q and high sediment concentration region can be observed (the sub-panels in (b) for enlarged view). It is evident that the inertia terms in the sediment velocity expression is responsible for the preferential concentration of sediment observed in Fig. 12(b).

In summary, two additional numerical experiments are carried out by increasing St, while keeping the other non-dimensional parameters the same as Case 0. Analysis of the mean profiles reveals that large particle inertia tends to attenuate flow turbulence. The well-known preferential concentration effect is illustrated using Case A3.

5.2. Gelling ignition

The unbounded resuspension of sediments in Case B4 is an interesting phenomenon, which may have profound implications on the fine sediment transport on continental shelves. Similar results are also reported by Kampf and Myrow (2014) using an eddy-viscosity based model, and it is named gelling ignition. Here, the more sophisticated turbulence-resolving simulation results are used to further investigate the occurrence of gelling ignition. The time-averaged deposition flux over one wave cycle $\overline{\widetilde{D}}$ is calculated and approximated as:

$$\overline{\widetilde{D}} = \widetilde{W}_{s0}\overline{\phi_b\left(1-\frac{\phi_b}{\phi_{ref}}\right)^m} \approx \widetilde{W}_{s0}\overline{\phi_b}\left(1-\frac{\overline{\phi_b}}{\phi_{ref}}\right)^m. \tag{25}$$

We need to point out that this approximation shown on the right-hand-side is only appropriate when the variation of bottom concentration during one wave cycle is small (see Fig. 9(b)). Since $m \neq 0$, the wave-averaged deposition flux is clearly a nonlinear

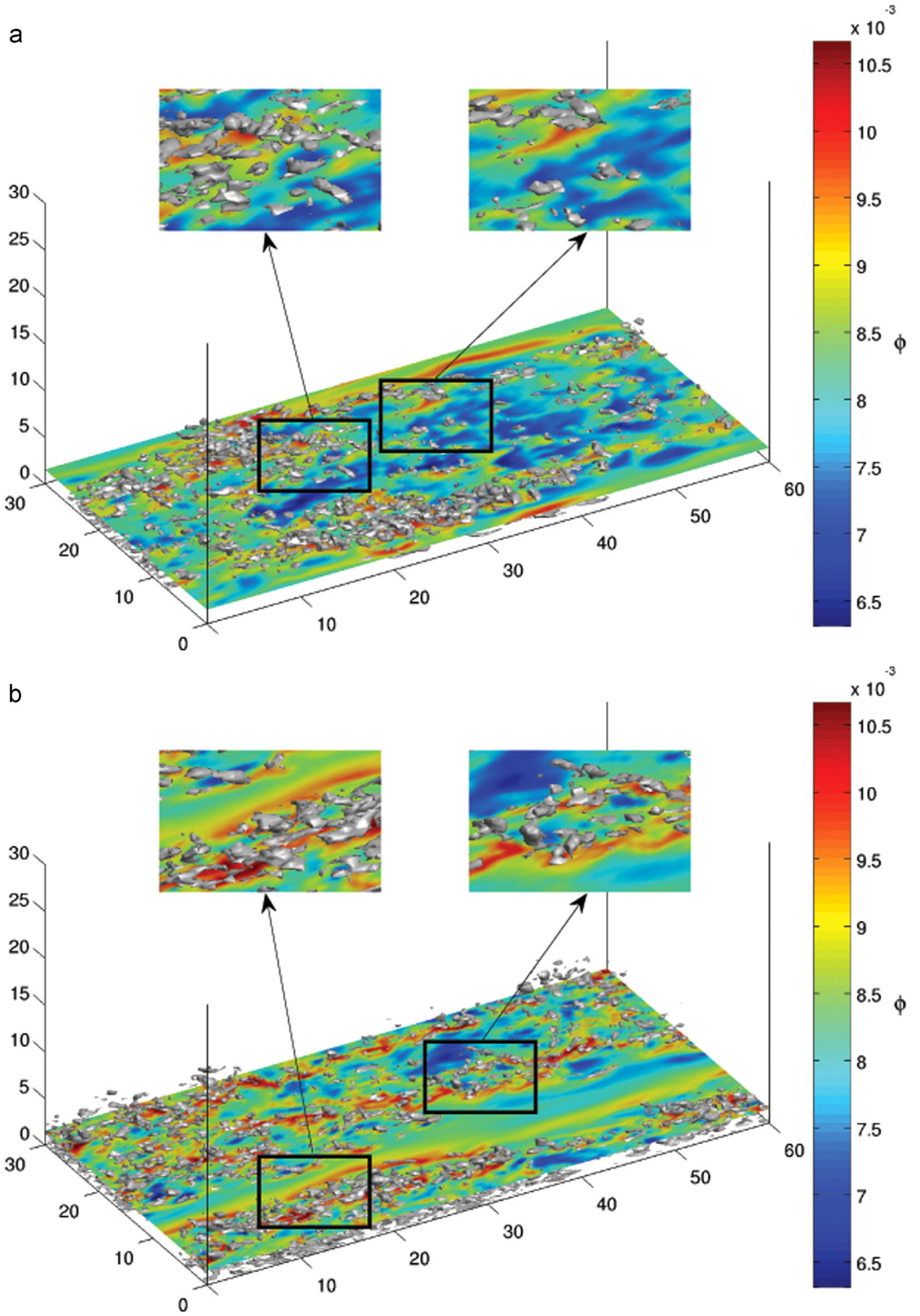

Fig. 12. Turbulent coherent structures at flow peak ($t=10$ T) for (a) Case 0 and (b) Case A3. The turbulent coherent structures are visualized using the second invariant Q, and the contour level used here is −0.04 (non-dimensional). The plane cuts of the concentration ϕ field at $z=1.5$ are also shown. The sub-panels show enlarged views for better visualization of the preferential concentration effect.

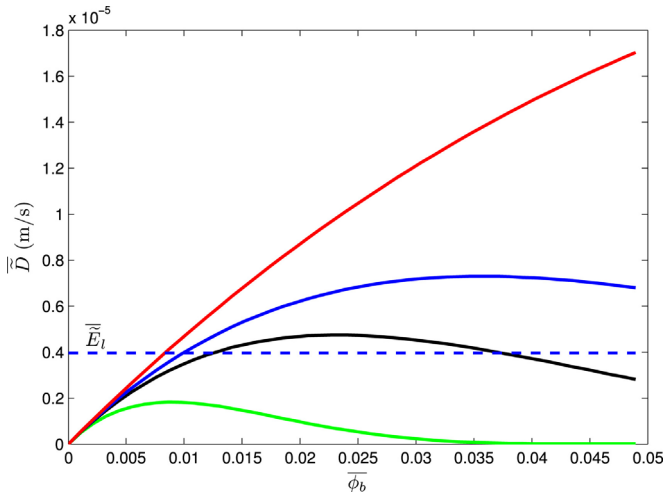

Fig. 13. Wave-averaged depositional flux $\overline{\widetilde{D}}$ as a function of wave-averaged bottom concentration $\overline{\phi_b}$ for Case B1 (circle symbols), Case B2 (curve with cross symbols), Case B3 (dash-dot curve) and Case B4 (thick solid curve). The dashed curve $\overline{\widetilde{E}}_l$ is the wave-averaged erosion flux at the bottom calculated using laminar solution of bottom shear stress at $Re_\Delta = 1000$ (Cheng et al., 2015). The dimensional value for the critical shear stress of erosion is $\tilde{\tau}_c = 0.02$ Pa for all the cases.

function of wave-averaged bottom sediment concentration that also depends on the reference (gelling) concentration ϕ_{ref}. In Fig. 13, $\overline{\widetilde{D}}$ is plotted against $\overline{\phi_b}$ with $m=4.6$ for four different ϕ_{ref} considered in this study. It is noted that for a given ϕ_{ref}, there exists a maximum $\overline{\widetilde{D}}$ and this maximum deposition flux is smaller for lower gelling concentration due to hindered settling effect.

On the other hand, the erosional flux averaged over one wave cycle is calculated as

$$\overline{\widetilde{E}} \approx \widetilde{m}_e\left(\frac{\overline{|\tilde{\tau}_b|}}{\tilde{\tau}_c} - 1\right), \tag{26}$$

where the approximation of the wave-averaged erosional flux is appropriate for relatively small critical shear stress (Cheng et al., 2015). Once the wave-averaged bottom shear stress $\overline{|\tilde{\tau}_b|}$ can be estimated, $\overline{\widetilde{E}}$ is determined. Two scenarios can be expected. If $\overline{\widetilde{E}}$ is lower than the maximum $\overline{\widetilde{D}}$, an equilibrium state exists, which corresponds to one of the interceptions between $\overline{\widetilde{E}}$ and $\overline{\widetilde{D}}$ (see Fig. 13). The transport mode of this equilibrium state is further determined by the degree of sediment-induced density stratification (Ozdemir et al., 2010; Cheng et al., 2015). On the other hand, if the erosion flux is always greater than the deposition flux, no equilibrium state exists, and this will further result in the unlimited resuspension, or gelling ignition, as observed previously.

Because sediments can attenuate the flow turbulence and hence reduce the bottom stress, in general it is not straightforward to estimate the wave-averaged bottom stress magnitude $\overline{|\tilde{\tau}_b|}$ in order to estimate $\overline{\widetilde{E}}$. Numerical simulation carried out in this study can provide information on bottom stress and $\overline{|\tilde{\tau}_b|}$ at the equilibrium state are shown as $\overline{\tilde{\tau}}_{eq}$ in Table 1. Because a large (or unlimited) supply of resuspended sediment is expected when gelling ignition occurs, laminarized transport mode III is surely to follow. Indeed, model results discussed here suggest when gelling ignition occurs in Case B4, $\overline{|\tilde{\tau}_b|}$ reduces to 0.28 Pa (Table 1), which is identical to the laminar solution at Stokes Reynolds number of $Re_\Delta = 1000$ (Cheng et al., 2015). The corresponding erosion flux $\overline{\widetilde{E}}_l$ associated with $\overline{|\tilde{\tau}_b|} = 0.28$ Pa is shown in Fig. 13 (see the dashed line). It is evident that the deposition flux associated with a gelling concentration of $\phi_{ref}=0.05$ is always lower than $\overline{\widetilde{E}}_l$ while for Cases B1, B2 and B3 with higher gelling (reference) concentration, there are always interceptions between $\overline{\widetilde{D}}$ and $\overline{\widetilde{E}}_l$.

Through the above analysis, we can see that the gelling ignition can be triggered by a low gelling (reference) concentration in the hindered settling model. When the gelling concentration is low enough, the deposition flux curve is always below the erosional flux line. Consequently, the net flux at the bottom boundary is always positive (net erosional), and more sediments are resuspended into the domain. In this process, although the flow is initially turbulent, as the sediment availability increases, the sediment-induced density stratification is enhanced. Eventually, the laminarized transport mode III is obtained. It is noted that even in the laminarized stage, the viscous suspension in the laminarized flow can keep sediment suspended. In reality, viscous suspension further depends on the closure of rheological stress, which is neglected here, and we parameterize the viscous suspension process simply with a constant Schmidt number $Sc=0.5$.

With findings learned so far, it is possible to propose a simple parameterization for the occurrence of the gelling ignition. We consider that the critical condition to initiate gelling ignition is when the wave-averaged erosion flux at equilibrium balances the maximum wave-averaged depositional flux. For the deposition/erosion formulations adopted here and the resulting wave-averaged form shown in Eqs. (25) and (26), the critical condition occurs at $\phi_b = \phi_{ref}/(m+1)$ with

$$\overline{\widetilde{D}}_{max} = \widetilde{W}_{s0}\phi_{ref}\frac{m^m}{(m+1)^{m+1}}. \tag{27}$$

By evaluating $\overline{\widetilde{E}} = \overline{\widetilde{D}}_{max}$ at equilibrium, we obtain

$$\phi_{ref} = \frac{\widetilde{m}_e}{\widetilde{W}_{s0}}\frac{(m+1)^{m+1}}{m^m}\left(\frac{\overline{|\tilde{\tau}_b|}}{\tilde{\tau}_c} - 1\right), \tag{28}$$

For cohesive sediments, this expression involves several empirical parameters associated with flocs, including the floc settling velocity $\widetilde{W}_{s0}$, and erodibility parameters $\widetilde{m}_e$ and $\tilde{\tau}_c$. It is reminded that the floc properties are assumed to be constant throughout the simulation, and the complexity of variable viscosity due to rheology is neglected. This assumption may not hold true in reality. Nevertheless, our model results provide the first step to understand the condition for the occurrence of gelling ignition. As demonstrated in this study, the gelling ignition is likely to occur near laminarization, we specify $\overline{|\tilde{\tau}_b|} = 0.28$ Pa as in the laminarized flow at Stokes Reynolds number $Re_\Delta=1000$. Using the values of $\widetilde{m}_e$ and $\widetilde{W}_{s0}$ identical to those used in the numerical simulations (see Table 1), a 2D map for the occurrence of gelling ignition as a function of critical shear stress of erosion and gelling (reference) concentration is shown in Fig. 14(a). The curve shown in Fig. 14 (a) represents Eq. (28) with $\overline{|\tilde{\tau}_b|} = 0.28$ Pa and the region below the curve signifies the occurrence of gelling ignition. The corresponding values for Cases B1–B4 are also plotted, and the prediction of Eq. (28) is consistent with the numerical results of this study for $Re_\Delta=1000$. Since the main flow variable in Eq. (28) is the wave-averaged bottom stress $\overline{|\tilde{\tau}_b|}$ and we have demonstrated that the laminar solution value is appropriate for the present purpose, we can further present the prediction formula of Eq. (28) for other (lower) Stokes Reynolds number by specifying $\overline{|\tilde{\tau}_b|}$ using the corresponding value obtained from the laminar solution (see Fig. 14 (b)). As mentioned before, the gelling concentration can be related to the fractal dimension n_f, and more porous, organic flocs tend to have lower n_f and hence lower gelling concentration. Fig. 14 (b) indicates that for cohesive sediment with lower critical shear stress of erosion $\tilde{\tau}_c$, gelling ignition can be triggered at higher gelling concentration (higher n_f). Moreover, when the oscillatory flow is more energetic (larger Re_Δ), the gelling ignition can also be triggered at higher gelling concentration (higher n_f).

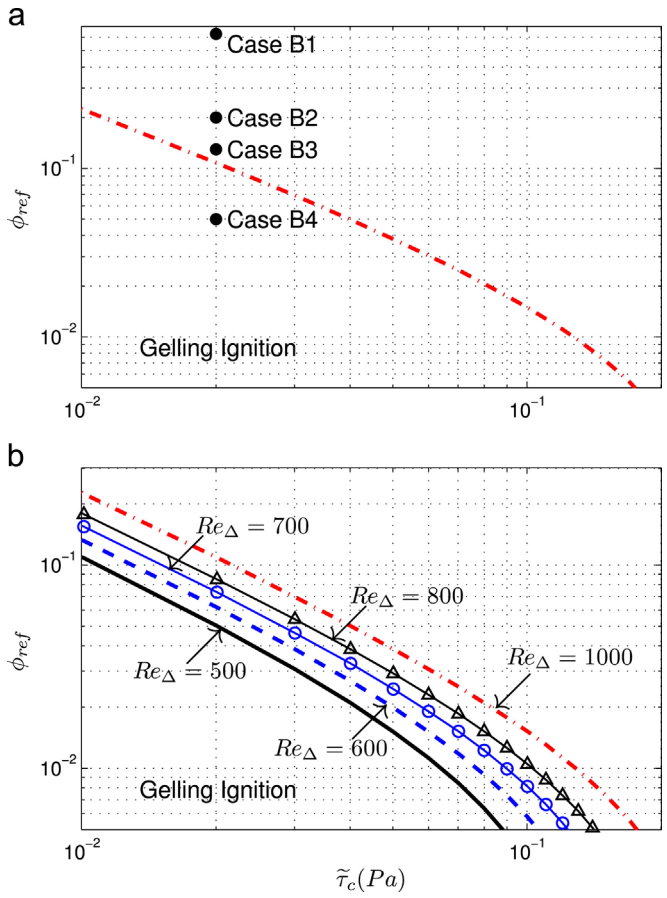

Fig. 14. (a) A predictor of gelling ignition as a function of dimensional critical shear stress $\tilde{\tau}_c$ and gelling concentration ϕ_{ref} at $Re_\Delta = 1000$. The black filled circles denote Cases B1–B4 in this study. (b) A predictor of gelling ignition as a function of $\tilde{\tau}_c$ and ϕ_{ref} at $Re_\Delta = 500$ (solid curve); $Re_\Delta = 600$ (dashed curve); $Re_\Delta = 700$ (curve with circle symbols); $Re_\Delta = 800$ (curve with triangle symbols); $Re_\Delta = 1000$ (dash-dot curve). All the results shown here are for $\widetilde{W}_s = 0.5$ mm/s and $\widetilde{m}_e = 3.05 \times 10^{-7}$ m/s.

6. Conclusion

In this study, the uncertainties due to model simplifications in sediment phase velocity, namely particle inertia and hindered settling for fine sediment transport in the wave boundary layer are investigated. Continuing the work of Cheng et al. (2015), fine sediment resuspension/deposition in the oscillatory boundary layer with Stokes Reynolds number $Re_\Delta = 1000$ is carried out by using a highly accurate turbulence-resolving model (Yu et al., 2013; Cheng et al., 2015). It is revealed that retaining the particle inertia at the Stokes number of $St = 0.03$, which corresponds to the value typical for fine sediment transport in energetic continental shelves, makes a very minor difference in the numerical results. Attenuation of flow turbulence is increased by no more than 10% by considering the particle inertia at $St = 0.03$ and the resulting transport mode is unchanged. Therefore, previous numerical studies neglecting the particle inertia effect at Stokes number up to 0.03 is justified. However, further numerical experiments with larger St reveal that particle inertia tends to damp flow turbulence, and the transport mode II in Case 0 shifts to transport mode III when the Stokes number St increases to 0.2.

At a fixed critical shear stress ($\tilde{\tau}_c = 0.02$ Pa) for erosion, the sediment availability in the domain is increased due to the reduced deposition flux by hindered settling. However, the degree of hindered settling is highly dependent on the reference (gelling) concentration used. For non-flocculated sediment with $\phi_{ref} = 0.63$, the increase of sediment availability is only about 10%, while the turbulence attenuation is slightly increased, no shift of transport modes is observed. However, when flocs of relatively high fractal dimension are considered, which results in $\phi_{ref} = 0.2$ and 0.13, more significant hindered settling effect enhances sediment availability, significantly attenuates flow turbulence and a laminarized transport mode III is obtained. After laminarization, an equilibrium state can be established with a balance between the depositional flux and the erosion flux due to viscous suspension. However, for more porous flocs of a low fractal dimension that gives $\phi_{ref} = 0.05$, we demonstrate that an equilibrium state cannot be achieved. An unlimited increase of sediment in the domain is obtained in the simulation because the depositional flux is always lower than the erosion flux. This unlimited sediment availability is caused by the gelling ignition as described in Kampf and Myrow (2014).

Simulations carried out in the previous studies (Ozdemir et al., 2010; Cheng et al., 2015) and this study show a bimodal behavior, in which large amount of fine sediments can be kept in suspension driven by an energetic wave condition at high gelling concentration ($\phi_{ref} = 0.63$) in the turbulent transport mode II and at very low gelling concentration in laminarized transport mode III as the gelling ignition is triggered. These findings provide critical insights into the formation and the fate of wave supported sediment-driven gravity flows.

Finally, a criterion for the occurrence of gelling ignition is proposed. From the theoretical perspective, we provide a framework of such criteria and demonstrate that the laminar solution can be used for the specification of bottom stress. However, we need to also note that other critical quantities related to floc structures, such as the Stokes settling velocity, erodibility parameters (e.g., $\tilde{\tau}_c$ and $\widetilde{m}_e$) and gelling concentration are still highly empirical and rely on in situ data. Characterizing and modeling those parameters for cohesive sediment is complex due to consolidation, sand content and bio-chemical effects, thus more future studies are needed.

Acknowledgments

This work is supported by National Science Foundation (OCE-1130217) and Office of Naval Research (N00014-14-1-0586) to the University of Delaware and National Science Foundation (OCE-1131016) to the University of Florida. Simulations presented in this paper are carried out on Chimera and Mills at the University of Delaware and the Extreme Science and Engineering Discovery Environment, which is supported by National Science Foundation Grant no. TG-OCE100015.

Appendix A. Top boundary treatment

In this section, we focus on the implementation of the top boundary condition for sediment concentration. To satisfy the mass conservation at the top boundary, the no-flux boundary condition (Eq. (7)) should be satisfied. Notice that the effective settling velocity may vary with x and y if hindered settling or particle inertia is considered. In the present numerical schemes, Fourier expansions are adopted in both streamwise and spanwise directions. If we transfer Eq. (7) into Fourier space, convolution terms will arise from the nonlinear multiplication term (first term on left-hand-side of Eq. (7)), which is difficult to handle. To resolve this problem, the sediment velocity at the top boundary is decomposed into x–y plane-averaged component $\langle w^s \rangle$ and the fluctuation component $w^{s'}$:

$$w^s = \langle w^s \rangle + w^{s'}. \tag{A.1}$$

Substituting Eq. (A.1) into Eq. (7) will result in

$$\langle w^s\rangle\phi - \frac{1}{Re_\Delta Sc}\frac{\partial\phi}{\partial z}\bigg|_{z=L_z} = -\,w^{s'}\phi|_{z=L_z}. \tag{A.2}$$

However, the sediment concentration ϕ on the right-hand-side of the above equation is part of the solution, to make sure that the top boundary has the same accuracy in terms of time integration, the right-hand-side term is approximated by using a second-order accurate scheme:

$$\phi^{(n_*)} = [1 + \frac{c(n)}{c(n-1)}]\phi^{(n-1)} - \frac{c(n)}{c(n-1)}\phi^{(n-2)}\bigg|_{z=L_z}, \tag{A.3}$$

where n denotes the time steps, and $c = \{dt/6, 5dt/24, dt/8\}$ is the coefficient for the diffusion term in the third-order low-storage Runge–Kutta method with dt being the time-step (Yu et al., 2013). In this study, the time step is chosen based on the Courant-Friedrichs-Lewy (CFL) criterion. $\phi^{(n_*)}$ is the approximation of ϕ at the bottom at the n step, and $\phi^{(n-1)}$ and $\phi^{(n-2)}$ are sediment concentration at the previous two time steps $(n-1)$ and $(n-2)$, respectively.

Appendix B. Supplementary data

Supplementary data associated with this paper can be found in the online version at http://dx.doi.org/10.1016/j.cageo.2015.07.009.

References

Arakawa, A., Lamb, V.R., 1981. A potential enstrophy and energy conserving scheme for the shallow water equations. Mon. Wea. Rev. 109 (January (1)), 18–36.

Balachandar, S., Eaton, J.K., 2010. Turbulent dispersed multiphase flow. Annu. Rev. Fluid Mech. 42, 111–133.

Berryman, J.G., 1983. Random close packing of hard spheres and disks. Phys. Rev. A 27 (February (2)), 1053–1061.

Bever, A.J., McNinch, J.E., Harris, C.K., 2011. Hydrodynamics and sediment-transport in the nearshore of Poverty Bay, New Zealand: observations of nearshore sediment segregation and oceanic storms. Cont. Shelf Res. 31 (April (6)), 507–526.

Cantero, M.I., Balachandar, S., Garcia, M.H., 2008. An Eulerian–Eulerian model for gravity currents driven by inertial particles. Int. J. Multiph. Flow 34 (May (5)), 484–501.

Chakraborty, P., Balachandar, S., Adrian, R.J., 2005. On the relationships between local vortex identification schemes. J. Fluid Mech. 535, 189–214.

Cheng, Z., Yu, X., Hsu, T.-J., Ozdemir, C.E., Balachandar, S., 2015. On the transport modes of fine sediment in the wave boundary layer due to resuspension/deposition: a turbulence-resolving numerical investigation. J. Geophys. Res. Oceans 120 (March (3)), 1918–1936.

Chorin, A.J., 1968. Numerical solution of the Navier–Stokes equations. Math. Comput. 22 (104), 745–762.

Cortese, T.A., Balachandar, S., 1995. High performance spectral simulation of turbulent flows in massively parallel machines with distributed memory. Int. J. High Perform. C 9 (3), 187–204.

Dankers, P., Winterwerp, J., 2007. Hindered settling of mud flocs: theory and validation. Cont. Shelf Res. 27 (August (14)), 1893–1907.

Dyer, K., Manning, A., 1999. Observation of the size, settling velocity and effective density of flocs, and their fractal dimensions. J. Sea Res. 41 (1), 87–95.

Fredsoe, J., Deigaard, R., 1992. Mechanics of Coastal Sediment Transport. Advanced Series on Ocean Engineering vol. 3. World Scientific, Singapore.

Geyer, W.R., Trowbridge, J.H., Bowen, M.M., 2000. The dynamics of a partially mixed estuary. J. Phys. Oceanogr. 30 (8), 2035–2048.

Hale, R., Ogston, A., Walsh, J., Orpin, A., 2014. Sediment transport and event deposition on the Waipaoa River Shelf, New Zealand. Cont. Shelf Res. 86 (September (0)), 52–65.

Harris, C.K., Wiberg, P., 2002. Across-shelf sediment transport: interactions between suspended sediment and bed sediment. J. Geophys. Res. 107 (January (C1)) 8-1–12.

Hedges, J., Keil, R., Benner, R., 1997. What happens to terrestrial organic matter in the ocean? Org. Geochem. 27 (November (5–6)), 195–212.

Hill, P.S., Milligan, T.G., Geyer, W., 2000. Controls on effective settling velocity of suspended sediment in the Eel River flood plume. Cont. Shelf Res. 20 (December (16)), 2095–2111.

Jensen, B., Sumer, B., Fredsoe, J., 1989. Turbulent oscillatory boundary layers at high Reynolds numbers. J. Fluid Mech. 206, 265–297.

Jimenez, J.A., Madsen, O.S., 2003. A simple formula to estimate settling velocity of natural sediments. J. Waterw. Port, Coast. Ocean Eng. 129 (2), 70–78.

Kampf, J., Myrow, P., 2014. High-density mud suspensions and cross-shelf transport: on the mechanism of gelling ignition. J. Sediment. Res. 84 (March (3)), 215–223.

Kniskern, T.A., Mitra, S., Orpin, A.R., Harris, C.K., Walsh, J., Corbett, D., 2014. Characterization of a flood-associated deposit on the Waipaoa river shelf using radioisotopes and terrigenous organic matter abundance and composition. Cont. Shelf Res. 86, 66–84.

Kolker, A.S., Li, C., Walker, N.D., Pilley, C., Ameen, A.D., Boxer, G., Ramatchandirane, C., Ullah, M., Williams, K.A., 2014. The impacts of the great Mississippi/Atchafalaya River flood on the oceanography of the Atchafalaya Shelf. Cont. Shelf Res. 86 (September (0)), 17–33.

Kranenburg, C., 1994. The fractal structure of cohesive sediment aggregates. Estuar. Coast. Shelf Sci. 39 (6), 451–460.

Lamb, M.P., D'Asaro, E., Parsons, J.D., 2004. Turbulent structure of high-density suspensions formed under waves. J. Geophys. Res. 109 (C12).

Ma, Y., Wright, L.D., Friedrichs, C.T., 2008. Observations of sediment transport on the continental shelf off the mouth of the Waiapu River, New Zealand: evidence for current-supported gravity flows. Cont. Shelf Res. 28 (4), 516–532.

Mehta, A., 1986. Characterization of cohesive sediment properties and transport processes in estuaries. In: Mehta, A. (Ed.), Lecture Notes on Coastal and Estuarine Studies vol. 14. Springer, New York, pp. 290–325.

Milliman, J.D., Farnsworth, K.L., 2011. River Discharge to the Coastal Ocean: A Global Synthesis. Cambridge University Press (ISBN: 9781107612181).

Noh, Y., Fernando, H., 1991. Dispersion of suspended particles in turbulent flow. Phys. Fluids A 3 (7), 1730–1740.

Ogston, A., Cacchione, D., Sternberg, R., Kineke, G., 2000. Observations of storm and river flood-driven sediment transport on the northern California continental shelf. Cont. Shelf Res. 20 (December (16)), 2141–2162.

Ozdemir, C.E., Hsu, T.-J., Balachandar, S., 2010. A numerical investigation of fine particle laden flow in an oscillatory channel: the role of particle-induced density stratification. J. Fluid Mech. 665, 1–45.

Ozdemir, C.E., Hsu, T.-J., Balachandar, S., 2011. A numerical investigation of lutocline dynamics and saturation of fine sediment in the oscillatory boundary layer. J. Geophys. Res. 116 (C9).

Pope, S.B., 2000. Turbulent Flows. Cambridge University Press, pp. 236–237 (ISBN: 978-0-521-59886-6).

Richardson, J., Zaki, W., 1954. Sedimentation and fluidisation. Part I. Trans. Inst. Chem. Eng. 32 (December), 35–53.

Ross, M.A., Mehta, A.J., 1989. On the mechanics of lutoclines and fluid mud. J. Coast. Res., 51–62.

Sahin, C., Safak, I., Sheremet, A., Mehta, A.J., 2012. Observations on cohesive bed reworking by waves: Atchafalaya Shelf, Louisiana. J. Geophys. Res. 117 (C9).

Sanford, L.P., Maa, J.P.-Y., 2001. A unified erosion formulation for fine sediments. Mar. Geol. 179 (1), 9–23.

Spalart, P.R., Baldwin, B.S., 1989. Direct simulation of a turbulent oscillating boundary layer. In: Turbulent Shear Flows, vol. 6, Springer, Berlin Heidelberg, pp. 417–440.

Sternberg, R., Cacchione, D., Paulso, B., Kineke, G., Drakez, D., 1996. Observations of sediment transport on the Amazon subaqueous delta. Cont. Shelf Res. 16 (5), 697–715.

Traykovski, P., Geyer, W., Irish, J., Lynch, J., 2000. The role of wave-induced density-driven fluid mud flows for cross-shelf transport on the Eel river continental shelf. Cont. Shelf Res. 20 (16), 2113–2140 (Oceanic Flood Sedimentation).

Traykovski, P., Trowbridge, J., Kineke, G., 2015. Mechanisms of surface wave energy dissipation over a high-concentration sediment suspension. J. Geophys. Res. Oceans 120 (March (3)), 1638–1681.

Traykovski, P., Wiberg, P., Geyer, W., 2007. Observations and modeling of wave-supported sediment gravity flows on the Po prodelta and comparison to prior observations from the Eel shelf. Cont. Shelf Res. 27 (February (3–4)), 375–399.

Trowbridge, J., Kineke, G., 1994. Structure and dynamics of fluid muds on the Amazon continental shelf. J. Geophys. Res. 99 (C1), 865–874.

Wang, L.-P., Maxey, M.R., 1993. Settling velocity and concentration distribution of heavy particles in homogeneous isotropic turbulence. J. Fluid Mech. 256, 27–68.

Winterwerp, J.C., 1998. A simple model for turbulence induced flocculation of cohesive sediment. J. Hydraul. Res. 36 (May (3)), 309–326.

Winterwerp, J.C., 2007. On the sedimentation rate of cohesive sediment. In: Maa, J. P.Y., Sanford, L., Schoellhamer, D. (Eds.), Estuarine and Coastal Fine Sediments Dynamics Intercoh 2003, vol. 8, Elsevier, 2003, pp. 209–226.

Winterwerp, J.C., Van Kesteren, W.G., 2004. Introduction to the Physics of Cohesive Sediment Dynamics in the Marine Environment. Elsevier.

Wright, L., Nittrouer, C., 1995. Dispersal of river sediments in coastal seas: six contrasting cases. Estuaries 18 (3), 494–508.

Wright, L.D., Wiseman, W.J., Bornhold, B.D., Prior, D.B., Suhayda, J.N., Keller, G.H., Yang, Z.-S., Fan, Y.B., 1988. Marine dispersal and deposition of Yellow River silts by gravity-driven underflows. Nature 332 (April (6165)), 629–632.

Yu, X., Hsu, T.-J., Balachandar, S., 2013. A spectral-like turbulence-resolving scheme for fine sediment transport in the bottom boundary layer. Comput. Geosci. 61 (December), 11–22.

Yu, X., Ozdemir, C., Hsu, T., Balachandar, S., 2014. Numerical investigation of turbulence modulation by sediment-induced stratification and enhanced viscosity in oscillatory flows. J. Waterw. Port, Coast. Ocean Eng. 140 (2), 160–172.

Zhou, J., Adrian, R.J., Balachandar, S., Kendall, T.M., 1999. Mechanisms for generating coherent packets of hairpin vortices in channel flow. J. Fluid Mech. 387, 353–396.